Title: ESRP1-Mediated Alternative Splicing During Oocyte Development is Required for Mouse Fertility

Running title: ESRP1 deletion causes female infertility in mice

Luping Yu[1], Huiru Zhang[1], Xuebing Guan[1], Dongdong Qin[1], Jian Zhou[2#], Xin Wu[1#]

[1]State Key Laboratory of Reproductive Medicine, Nanjing Medical University, Nanjing, Jiangsu 210029, China

[2]Department of Pediatric Laboratory, Wuxi Children's Hospital Affiliated to Nanjing Medical University, Wuxi, Jiangsu 214023, China

[#]Correspondence and requests for materials should be addressed to Dr. Xin Wu (email: xinwu@njmu.edu.cn) or Dr. Jian Zhou (jianzhou@njmu.edu.cn)

Abstract

Alternative splicing (AS) contributes to gene diversification in cells, but the importance of AS during germline development remains largely undefined. Here, we interrupted pre-mRNA splicing events controlled by epithelial splicing regulatory protein 1 (ESRP1) and found that it induced female infertility in mice. Germline-specific knockout of *Esrp1* perturbed spindle organization, chromosome alignment, and metaphase-to-anaphase transformation in oocytes. The first polar body extrusion (PBE) was blocked during oocyte meiosis and was found to be due to abnormal activation of spindle assembly checkpoint (SAC) and insufficiency of anaphase-promoting complex/cyclosome (APC/C) in *Esrp1*-knockout oocytes. *Esrp1*-knockout in oocytes hampered follicular development and ovulation; eventually, premature ovarian failure (POF) occurred in six-month-old *Esrp1*-knockout mouse. Using single-cell RNA sequencing analysis, 528 aberrant AS events of maternal mRNA transcripts were revealed and were preferentially associated with microtubule cytoskeletal organization in *Esrp1*-knockout oocytes. Notably, we found that loss of ESRP1 disturbed a comprehensive set of gene-splicing sites—including those within *Trb53bp1*, *Rac1*, *Bora*, *Kif2c*, *Kif23*, *Ndel1*, *Kif3a*, *Cenpa*, and *Lsm14b*—that ultimately caused abnormal spindle organization. Taken together, our findings provide the first report elucidating the AS program of maternal mRNA transcripts, mediated by the splicing factor, ESRP1, that is required for oocyte meiosis and female fertility in mice.

Keywords: ESRP1, oocyte, alternative splicing, meiosis, female fertility

60 **Introduction**

61 Alternative splicing (AS) of pre-mRNA is a key step that gives rise to functionally
62 distinct proteins from a single gene, according to the developmental or physiological
63 state of cells in multicellular organisms. Variability in splicing patterns is a major
64 source of protein diversity from the genome (Black 2000). Nearly 95%, 60%, and 25%
65 of genes in humans, *Drosophila melanogaster*, and *Caenorhabditis elegans*,
66 respectively (Wang et al. 2008; Graveley et al. 2011; Ramani et al. 2011), undergo
67 alternative splicing based on RNA sequencing. Thus, AS significantly expands the
68 forms and functions of the genomes of organisms with limited numbers of genes
69 (Nilsen and Graveley 2010). Aberrations in splicing patterns have been implicated in
70 a number of different diseases; for example, abnormal splicing patterns of fibroblast
71 growth factor receptor 2 (*Fgfr2*) result in inner-ear developmental defects and hearing
72 loss (Rohacek et al. 2017). Additionally, aberrations in the splicing patterns of
73 G-protein-coupled receptor 137 (*Gpr137*) impair epithelial cell integrity and
74 contribute to intestinal pathogenesis (Mager et al. 2017). However, the involvement of
75 AS regulation in germline cell development has not been well elucidated.

76 The mammalian oocyte represents a unique physiological case because it exhibits
77 high transcriptional activity during growth, followed by transcriptional quiescence
78 when it is stimulated to resume meiosis. In non-surrounded nucleolus (NSN)-type
79 oocytes, chromatin does not surround the nucleolus, and gene transcription is globally
80 active; in contrast, in surrounded nucleolus (SN)-type oocytes, chromatin is highly
81 condensed and gathered around the nucleolus, and gene transcription is globally
82 silenced (Kageyama et al. 2007). Oocytes rely on the storage of maternal transcripts
83 to maintain cellular processes throughout meiotic maturation and cytoplasmic
84 maturational events that provide competence for fertilization and embryogenesis.
85 Thus, a specific post-transcriptional regulatory context has increased importance in
86 oocytes and is essential to generate high-quality female gametes (Sha et al. 2019;
87 Christou-Kent et al. 2020). At present, some evidence has suggested that alternative

88 pre-mRNA splicing significantly contributes to accurate control of maternal
89 transcripts (Do et al. 2018; Kasowitz et al. 2018). However, the landscape of
90 pre-mRNA splicing within the stored RNA pool in oocytes has not yet been critically
91 examined.

92 RNA-binding proteins (RBPs) control the fate of RNAs with one or more
93 RNA-recognition motif (RRM) domains and accessory domains, which participate in
94 many post-transcriptional processes, including the splicing of pre-mRNA, as well as
95 ensuring the localization and stability of RNAs within the cell (Hentze et al. 2018).
96 Epithelial splicing regulatory protein 1 (ESRP1) is preferentially known as an
97 epithelial-specific RBP that is composed of three RRM domains and regulates AS by
98 directly binding specific GU-rich sequence motifs in pre-mRNAs, and plays a role in
99 the epithelial-cell-specific splicing program (Warzecha et al. 2009b; Warzecha et al.
100 2010). ESRP1 also acts to maintain an epithelial-cell state by preventing the switch
101 from CD44 variant isoforms (CD44v) to the standard isoform (CD44s), which is
102 critical for regulating the epithelial-to-mesenchymal transition (EMT) and the
103 progression of breast cancer (Brown et al. 2011). ESRP1 has been demonstrated to
104 play essential roles in mammalian development through AS to maintain epithelial-cell
105 properties (Bebee et al. 2015). However, the physiological role of ESRP1 in the
106 maternal transcriptome in germline development has not yet been investigated. In the
107 present study, we found that ESRP1-mediated AS was required for spindle
108 organization, chromosome congression, meiotic progression, follicular development,
109 and ovulation in mouse oocytes. Loss of ESRP1 led to arrest of mouse meiotic
110 progression, ovulation disorders, premature ovarian failure, and female infertility.
111
112
113
114
115

116 **Results**

117 ***Esrp1* knockout leads to female infertility in mice**

118 A recent study used RBP capture to identify a set of RBPs with uncharacterized roles
119 in mammalian germline cells, including ESRP1 (Du et al. 2020). Here, we validated
120 the presence of ESRP1 in adult mouse stomach, lung, and kidney tissues (Fig. 1A).
121 ESRP1 was also detectable in prepubertal mouse testes, while highly enriched
122 expression of ESRP1 was found in mouse ovaries and at all follicular stages (Figs. 1A
123 and S1A). Because ESRP1 is required for mouse craniofacial development and
124 postnatal viability (Bebee et al., 2015), we next generated a conditional inactivation of
125 the *Esrp1* gene using the Cre/loxP system to investigate the functional roles of *Esrp1*
126 during germline development. In our experiments, the targeting construct contained
127 three loxP sites inserted into intron 6 and intron 9 of the *Esrp1* gene and one floxed
128 hygromycin and thymidine kinase (HyTK) double-selection cassette. All three loxP
129 sites were in the same orientation (Fig. S2A). Mice carrying the floxed allele
130 ($Esrp1^{fl/fl}$) were backcrossed with *Ddx4-Cre* mice (cat. #J006954, Jackson Laboratory)
131 to produce mice with germ-cell-specific inactivation of *Esrp1* in primordial germ cells
132 (PGCs) starting at embryonic day 12.5 (designated hereafter as $Esrp1^{fl/\triangle}$/*Ddx4-Cre*;
133 mouse-mating strategies are illustrated in Fig. S2B). We first found that
134 *Esrp1*-knockout male mice were grossly normal in terms of the morphology and size
135 of the testes and epididymis, as compared to those of wild-type mice (Fig. 1B). Next,
136 morphological analysis indicated that there were no apparent changes in
137 spermatogenesis at any stages of the seminiferous tubules in eight-week-old $Esrp1^{fl/\triangle}$
138 /*Ddx4-Cre* mouse testes (Fig. S1B). Furthermore, there was no significant decrease in
139 male fertility (Fig. 1C); however, females were completely infertile (Fig. 1G), as
140 indicated by the results of our breeding experiments from *Esrp1*-knockout mice.
141 Collectively, these data suggest that loss of ESRP1 in germline cells led to female
142 infertility, whereas such loss was dispensable for male fertility in mice.
143

144 **Follicular developmental defects and POF in *Esrp1*- knockout mouse**

145 In order to elucidate the requirement of postnatally expressed ESRP1 for female
146 fertility, we bred *Esrp1*$^{fl/fl}$ mice with male transgenic (Tg) mice
147 [Tg(*Gdf9*-icre)5092Coo, cat. #J011062, Jackson Laboratory] to inactivate the *Esrp1*
148 gene in oocytes starting at the primordial follicle at postnatal day 3 (PD3) (designated
149 hereafter as *Esrp1*$^{fl/fl}$*/Gdf9-Cre*, Fig. 1D) (Lan et al. 2004), following our previous
150 breeding strategies (Fig. S2B). ESRP1 protein was not detectable in *Esrp1* mutant
151 oocytes from *Esrp1*$^{fl/fl}$*/Gdf9-Cre* mouse ovaries (Fig. 1E), and immunofluorescent
152 analysis showed that ESRP1 was absent in primordial oocytes of *Esrp1*$^{fl/fl}$*/Gdf9-Cre*
153 ovaries and at all stages of subsequent oocytes (Fig. 1F). As we expected, no
154 pregnancies in female mice and no progeny were observed when *Esrp1*$^{fl/fl}$*/Gdf9-Cre*
155 female mice were bred with wild-type males, as comparing to results in *Esrp1*$^{fl/fl}$
156 female mice that produced approximately eight to nine pups per litter and
157 approximately six litters per female during six-month breeding periods (Fig. 1G).

158 Next, we examined the gross morphology of ovaries at different ages and
159 analyzed the composition of follicles according to the classifications of primordial,
160 primary, early-secondary, later-secondary, antral follicles, and the corpus luteum.
161 Follicle development was quantified to explore the reproductive function of female
162 mice, and we found that *Esrp1*$^{fl/fl}$*/Gdf9-Cre* ovaries were smaller in size compared to
163 *Esrp1*$^{fl/fl}$ ovaries from PD28 (Fig. 2A, D, G, J). The total number of follicles in
164 *Esrp1*$^{fl/fl}$*/Gdf9-Cre* ovaries was significantly lower compared to those in *Esrp1*$^{fl/fl}$ mice
165 at all stages (Fig. 2O). At PD28, there were fewer later-secondary and antral follicles
166 (Fig. 3C'); from PD60, follicles at all stages were dramatically reduced due to follicle
167 atresia (Fig. 2F', I', O); at PD180, nearly all follicles were absent except for a few
168 primary, secondary, and antral follicles that were found in *Esrp1*$^{fl/fl}$*/Gdf9-Cre* mouse
169 ovaries (Fig. 2K, L, L'). Different from control ovaries, the layers of cumulus cells
170 and mural granulosa cells (MGC) were significantly thinner at later-secondary and
171 antral follicles in *Esrp1*- knockout ovaries (Figs. 2B, C, E, F, H, I, arrows and inserts),

172 indicating that ESRP1 in oocyte was required for follicular development but may not
173 be necessary for the transition of primordial oocytes to the activated growing oocyte
174 stage. Notably, the corpus luteum was significantly less in *Esrp1*- knockout ovaries
175 compared to that in *Esrp1*$^{fl/fl}$ ovaries from PD28 to PD180 (Fig. 2C', F', I', L'),
176 suggesting that ovulation was impaired in *Esrp1*- knockout mice. We also
177 administered intraperitoneal injections of pregnant mare serum gonadotropin (PMSG)
178 and human chorionic gonadotropin (hCG) at 44–46 h after PMSG treatment to induce
179 ovulation in six-week-old mice. In contrast to results in *Esrp1*$^{fl/fl}$ oocytes, histological
180 analysis of cumulus-oocyte complexes (COCs) ovulated in mouse oviducts showed
181 that *Esrp1*- knockout oocytes did not extrude the first polar body (PB1) (Fig. 2M, N).
182 Therefore, oocytes in *Esrp1*$^{fl/fl}$*/Gdf9-Cre* mice lacked the competence to undergo
183 meiotic maturation. These results suggest that ESRP1 was required for follicular
184 development, ovulation and oocyte maturation in mice.
185
186 **Loss of ESRP1 induces oocyte meiotic arrest at metaphase I**
187 Next, we looked for possible defects during oocyte development in *Esrp1*$^{fl/fl}$*/Gdf9-Cre*
188 female mice. Using superovulation experiments, we first found an average of
189 approximately twenty-five ovulated oocytes in *Esrp1*$^{fl/fl}$ females after 16 h of hCG
190 treatments (Fig. 3B); however, the ovulation rate in *Esrp1*$^{fl/fl}$*/Gdf9-Cre* females was
191 significantly reduced to an average of approximately fourteen oocytes (Fig. 3B). In
192 contrast to normal oocytes ovulated from *Esrp1*$^{fl/fl}$ ovaries, displaying the PB1 and a
193 typical MII spindle (Fig. 3A, upper panel, differential interference contrast and
194 immunofluorescence staining, white arrow indicated) in mature MII-stage oocytes,
195 almost all of the ovulated oocytes from *Esrp1*$^{fl/fl}$*/Gdf9-Cre* ovaries had undergone
196 germinal vesicle breakdown (GVBD) with a spindle that had migrated to the cortex
197 but lacked the PB1 (Fig. 3A, low panel). The polar body extrusion (PBE) percentage
198 in *Esrp1*$^{fl/fl}$*/Gdf9-Cre* females was significantly decreased compared to that in
199 *Esrp1*$^{fl/fl}$ females (Fig. 3C). Next, we explored whether the defects in oocyte

200 development found *in vivo* could be reproduced through *in-vitro* maturation (IVM)
201 experiments. We first found that *Esrp1*- knockout oocytes had successive occurrences
202 of GVBD within 4 h, but with many lagged chromosomes and the percentage of
203 GVBD oocytes was reduced after 4 h (Fig. 3E). Importantly, only 6 in total 710
204 oocytes were found PBE after 16 h during IVM in *Esrp1*$^{fl/fl}$*/Gdf9-Cre* females, while
205 82.09% *Esrp1*$^{fl/fl}$ oocytes had entered into the metaphase-II stage, as characterized by
206 visible PB1 and univalent sister chromatids (Figs. 3D, E, S3A, B). None of the
207 *Esrp1*$^{fl/fl}$*/Gdf9-Cre*-ovulated oocytes underwent successful fertilization and developed
208 into blastocysts after *in-vitro* fertilization (IVF) with normal sperm (Fig. S3C). Using
209 chromosome-spread assay (Hodges and Hunt 2002), we further analyzed chromosome
210 morphology in ovulated oocytes from *Esrp1*$^{fl/fl}$/Gdf9-Cre mice. Oocytes from *Esrp1*$^{fl/fl}$
211 mice displayed the typical monovalent MII-stage chromosome array (pairs of sister
212 chromatids juxtaposed near their centromeres), whereas *Esrp1*$^{fl/fl}$*/Gdf9-Cre* oocytes
213 had intact bivalents with no homologue separation (Fig. 3F). These observations
214 strongly indicate that *Esrp1*- knockout oocytes were arrested at metaphase I with
215 inseparable homologous chromosomes.
216
217 **ESRP1 deficiency hampers spindle/chromosome organization and K-MT**
218 **attachments**
219 Next, we investigated whether defects occurred in spindle/chromosome organization
220 therefore contributed to metaphase-I arrest in *Esrp1*$^{fl/fl}$*/Gdf9-Cre* oocytes. We found
221 that the incidence of spindle defects and chromosome misalignments were
222 significantly higher in *Esrp1*$^{fl/fl}$*/Gdf9-Cre* ovulated oocytes than in *Esrp1*$^{fl/fl}$ oocytes
223 (94.05% ± 1.62% vs. 15.02% ± 1.75%; spindles in *Esrp1*- knockout oocytes retained
224 the barrel-shape characteristic of metaphase I even at ovulated oocytes considered to
225 have abnormal spindle/chromosome organization, Fig. 4A, B). Compared to *Esrp1*$^{fl/fl}$
226 oocytes (typical barrel-shaped MII spindles with organized chromosomes at the
227 equator), a large portion of *Esrp1*- knockout oocytes (48.86%) contained abnormal

228 spindle/chromosome organization with apparent monopolar spindle attachments
229 (either single or multiple chromosomes); 39.77% of oocytes with MI arrest spindles;
230 9.09% of oocytes exhibited catastrophic spindle disorganization and severely
231 misaligned chromosomes and 2.27% of oocytes had multiple spindles (Fig. 4A, C).
232 These results indicate that ESRP1 was required for spindle organization and
233 chromosome alignment during meiosis in mice.
234 On meiotic entry, dynamic microtubules form a bipolar spindle, which is
235 responsible for capturing and congressing chromosomes. These events require proper
236 attachment of kinetochores to microtubules emanating from opposite spindle
237 poles(Touati et al. 2015). We investigated whether kinetochore-microtubule (K-MT)
238 interactions were compromised resulting in defects contributed to
239 spindle/chromosome organization in *Esrp1*- knockout oocytes. To do this, metaphase
240 I oocytes were labeled with α-tubulin to visualize spindle and CREST to detect
241 kinetochores, and co-stained with DAPI for chromosomes (Fig. 4D, E). We found that
242 the majority K-MT pattern in normal oocytes is amphitelic attachment (the
243 kinetochore of one chromosome is connected to the spindle pole and the kinetochore
244 of the other chromosome is connected to the opposite spindle pole; Fig. 4 D, F,
245 chromosomes labeled 1 and 2). By contrast, the proportion of amphitelic K-MT
246 attachment was significantly reduced and the frequency of misattachments was
247 significantly increased in *Esrp1*- knockout oocytes relative to control (Fig. 4F),
248 including lost attachment (kinetochore attached to neither pole; Fig.4E, chromosomes
249 labeled 3 and 4), monotelic attachment (Fig. 4E, chromosomes labeled 5 and 6),
250 mix/undefined attachment (Fig. 4E, chromosome labeled 7), as well as merotelic
251 attachment (one kinetochore attached to both poles; Fig. 4E, chromosomes labeled 8).
252 The results indicate that the erroneous K-MT attachments could result in chromosome
253 alignment failure observed in *Esrp1*- knockout oocytes. Together, ESRP1 is essential
254 for K-MT interactions during oocyte meiotic maturation .
255 **ESRP1 deficiency activates the SAC and induces insufficient APC/C activity**

256 The spindle assembly checkpoint (SAC) ensures correct chromosome alignment
257 during meiosis (Overlack et al. 2015). Since *Esrp1*$^{fl/fl}$*/Gdf9-Cre* oocytes failed to
258 complete meiosis-I division and exhibited severe spindle- organization defects and
259 abnormal chromosome alignments, we next evaluated the activity of the SAC in
260 *Esrp1*- knockout oocytes. We analyzed the levels of BubR1, a principal component of
261 the SAC in oocytes. Oocytes collected from *Esrp1*$^{fl/fl}$ and *Esrp1*$^{fl/fl}$*/Gdf9-Cre* mice
262 were used to evaluate the SAC activity at 4 h and 6 h after GVBD (the time points
263 presenting oocytes at premetaphase-I (pre-MI) and metaphase-I (MI) stages,
264 respectively). In *Esrp1*$^{fl/fl}$ oocytes, BubR1 was localized to kinetochores during
265 pre-MI, and then degenerated during MI when kinetochores had become properly
266 attached to microtubules (Fig. 5A, B). In contrast, the BubR1 signal on kinetochores
267 was dramatically increased in *Esrp1*- knockout MI oocytes (Fig. 5A, B), suggesting
268 that SAC was activated.
269 Complete activation of anaphase-promoting complex/cyclosome (APC/C)
270 requires fulfillment of the SAC (Holt et al. 2013; Touati and Wassmann 2016). Since
271 we found that the SAC was abnormally activated in *Esrp1*- knockout oocytes, we next
272 asked whether MI arrest in *Esrp1*- knockout oocytes was due to insufficient APC/C
273 activity. We collected 10-h cultured oocytes from *Esrp1*$^{fl/fl}$ and *Esrp1*$^{fl/fl}$*/Gdf9-Cre*
274 females and assessed the protein levels of cyclin B1 and securin, two substrates of
275 APC/C, to evaluate APC/C activity of oocytes during the metaphase-to-anaphase
276 transition (Thornton and Toczyski 2003). In *Esrp1*$^{fl/fl}$ oocytes, both proteins were
277 nearly undetectable; however, in *Esrp1*- knockout oocytes, both proteins were present
278 during the metaphase-to-anaphase transition (Fig. 5C), suggesting that there was no
279 effective APC/C activity for cyclin B1 and securin degradation, rendering *Esrp1*-
280 knockout oocytes unable to enter into anaphase. Therefore, the SAC surveillance
281 mechanism and APC/C activity might represent major pathways mediating the effects
282 of loss of ESRP1 on meiotic progression in oocytes.
283 **Inhibition of SAC activity rescues defects of metaphase-I arrest induced by**

284 **ESRP1 deficiency**

285 Since we found that conditional knockout of *Esrp1* led to SAC activity during MI and
286 led to insufficient APC/C activity, we next investigated whether direct interference of
287 SAC activity during MI could rescue the phenotype of *Esrp1*- knockout oocytes. We
288 treated *Esrp1*- knockout oocytes with reversine (Fig. 6A), which inhibits the SAC
289 kinase, MPS1 (Santaguida et al. 2010). Reversine accelerate meiosis I progression in
290 $Esrp1^{fl/fl}$ oocytes and the PBE rate is adjusted to 100% 2h after reversine added, as
291 previously shown (Sha et al. 2018; Zhang et al. 2020) (Fig. 6B, C, D). Surprisingly,
292 reversine partially rescued metaphase I arrest caused by *Esrp1* deficiency and led to
293 the PB1 extrusion (Fig. 6B, C, D). The PB1 extrusion was confirmed by
294 immunofluorescence assay (Fig. 6E). The recovered PB1 extrusion, characterized by
295 homologous chromosome separation and disappearance of bivalent chromosomes,
296 was confirmed by chromosome-spread assay (Fig. 6F). Therefore, we conclude that
297 inhibition of SAC activity rescued metaphase-I arrest caused by *Esrp1* deficiency.
298

299 **Preferential nuclear-localized ESRP1 is involved in oocyte mRNA processing**

300 We next used oocytes from PD5, as well as PD12 ovaries and adolescent mice
301 pre-treated with PMSG for 44–46 h that were allowed to mature *in vitro* for 0, 8, and
302 14 h (corresponding to the GV-NSN/SN, MI, and MII stages, respectively), to
303 examine the subcellular localization of ESRP1 during each oocyte maturation stage.
304 ESRP1 was found to be preferentially localized to the nucleus in PD5, PD12, and
305 GV-NSN oocytes when transcription was active, but relatively low ESRP1 levels
306 were found in GV-SN, MI, and MII oocytes when transcription was inactive (Fig. 7A).
307 Next, using alkyne-modified nucleoside 5-ethynyl uridine (5-EU), which reflects
308 newly synthesized RNAs and global RNA synthesis, we found that 5-EU staining in
309 NSN-type oocytes was colocalized with high levels of ESRP1 in the nucleus, whereas
310 5-EU was undetectable in SN-type oocytes, and low levels of ESRP1 were found in
311 the cytoplasm (Fig. 7B), suggesting that ESRP1 was involved in mRNA processing

312 during oocyte maturation.

313 We next investigated the regulatory effects of ESRP1 and global RNA changes
314 due to ESRP1 knockout in mouse oocytes. Transcriptomes were compared in ovulated
315 oocytes between six-week-old *Esrp1*$^{fl/fl}$ and *Esrp1*$^{fl/fl}$*/Gdf9-Cre* females via
316 high-throughput sequencing (RNA-seq; four biological replicates in each group, GEO
317 database GSE149355). Approximately 85% of clean reads were applied for analyses
318 (Fig. S4A), and proximal values of global gene expression were shown within
319 samples (Fig. S4B). We found that 3,002 genes (1586 downregulated and 1416
320 upregulated) showed significant differences (FDR value < 0.01, more than 1.5-fold
321 and baseMeand ⩾10) in transcript levels between *Esrp1*$^{fl/fl}$ and *Esrp1*$^{fl/fl}$*/Gdf9-Cre*
322 (Table S3). Among them, numerous oocyte meiosis-related genes were
323 downregulated in *Esrp1-* knockout ovulated oocytes including *Ccnb1 (cyclin B1),*
324 *Ccnb3 (cyclin B3), Marf1, Pcnt, Dazl, Kif1b, Rab8b,* and *Spire1,* while some genes
325 involved in anaphase-I transformation—such as *Bub3* and *Pttg1 (Securin)*—were
326 upregulated (Fig. S4C). We further validated mRNA levels via quantitative real-time
327 PCR (qRT-PCR) in oocytes (Fig. S4D). We found that mRNA levels of genes
328 important for oocyte meiosis were significantly altered due to the conditional deletion
329 of *Esrp1* in mouse oocytes.

330 ESRP1 has been reported to functionally regulate AS (Warzecha et al. 2009b;
331 Bebee et al. 2015; Mager et al. 2017). Hence, we next analyzed global AS events
332 between *Esrp1*$^{fl/fl}$ and *Esrp1*$^{fl/fl}$*/Gdf9-Cre* oocytes via comprehensive AS hunting
333 method (CASH) (Wu et al. 2018). We revealed that 528 AS events from a total of
334 76,116 splicing events were affected in *Esrp1-* knockout oocytes (FDR value < 0.05,
335 Table S4). Our analysis revealed that the major cluster of splicing events was cassette
336 exon (230) among the 528 AS events, while others included alternative start exon
337 (107), alternative end exon (70), multiple adjacent cassette exons (35), intron
338 retention (31), alternative 5' splice site (20), mutually exclusive exons (19), and
339 alternative 3' splice site (16) (Fig. 7C). These AS events occurred in a total of 459

340 genes and were subjected to Gene Ontology analysis. Microtubule cytoskeletal
341 organization was the top-affected biological process following *Esrp1* deletion, along
342 with organelle localization, actin cytoskeletal organization, and
343 establishment/maintenance of cellular polarity (Fig. 7D). Similarly, Kyoto
344 Encyclopedia of Genes and Genomes (KEGG) pathway analysis further suggested
345 that abnormal spindle organization in *Esrp1*- knockout oocytes was likely due to
346 aberrant AS in genes associated with cytoskeletal organization (Fig. 7D).
347

348 **Pre-mRNA splicing of spindle- organization- associated genes is required for**
349 **oocyte meiosis**

350 Using GV-stage and ovulated oocytes from *Esrp1*$^{fl/fl}$ and *Esrp1*$^{fl/fl}$*/Gdf9-Cre* females,
351 we next looked for splicing events due to *Esrp1* deletion. We confirmed that the three
352 exons of *Esrp1* were deleted completely in oocytes, as indicated in *Gdf9-Cre* mice
353 (Fig. 8A). A previous study reported that ESRP1 mediates splicing of *Fgfr2*
354 pre-mRNA (Warzecha et al. 2009a). In our present study, an identical splicing defect
355 of *Fgfr2* (termed mutually exclusive exons) was found in *Esrp1*$^{fl/fl}$*/Gdf9-Cre* oocytes
356 (Fig. 8A). Microtubule cytoskeletal organization has been shown to represent the key
357 step during mouse oocyte meiosis to maintain normal chromosome alignment and
358 spindle formation (Bennabi et al. 2016), and it is the most affected cellular process
359 due to deletion of *Esrp1* in oocytes. Therefore, we next selected nine genes that have
360 previously been shown to be associated with spindle organization during oocyte
361 meiosis for further analysis. We employed Integrative Genomics Viewer (IGV), a
362 visualization tool for efficient and flexible exploration of large and complicated data
363 sets obtained from sequencing (Robinson et al. 2011), to analyze ESRP1-mediated AS
364 of these nine genes. Among these AS events, *Trp53bp1, Rac1, Bora, kif23, Ndel1,*
365 *kif3a, Cenpa*, and *Lsm14b* were classified as cassette exon, whereas *kif2c* was an
366 alternative 5' splice site (Fig. 8A). Next, we used specific primers (Table S1) of target
367 genes and semi-quantitative PCR to determine the aberrant splicing patterns of these

368 nine genes in GV-stage and ovulated oocytes from *Esrp1*$^{fl/fl}$ and *Esrp1*$^{fl/fl}$*/Gdf9-Cre*
369 females (Fig. 8B), which represent two key developmental stages during mouse
370 oocyte development. Among the nine genes, the splicing changes of *Lsm14b* were the
371 most obvious according to IGV and CASH analyses (Fig 8A and Table S4); LSM14B
372 directly binds to tubulin, and is essential for spindle stability and oocyte meiosis (Mili
373 et al. 2015; Zhang et al. 2017), so we use antibody to verify the protein change.
374 Strikingly, as revealed by Western blotting, ESRP1 depletion led to an obvious shift
375 from the standard isoform of LSM14B to the longer isoform of LSM14B (Fig. 8C). In
376 *Esrp1*$^{fl/fl}$ oocytes, there were two ESRP1-dependent splicing events in *Lsm14b*,
377 including the sixth exon (predominant) and the fourth exon skipped (Fig. 8A, B);
378 however, it was retained in *Esrp1*$^{fl/fl}$*/Gdf9-Cre* oocytes (Fig. 8A, B). In *Esrp1*$^{fl/fl}$ mice,
379 both isoforms of LSM14B proteins were found in GV-stage oocytes, and the standard
380 isoform was predominant. In contrast, in *Esrp1*- knockout oocytes, the protein levels
381 of two isoforms of LSM14B were dramatically shifted at the GV stage. This shift was
382 also confirmed in ovulated oocytes (Fig. 8C). The expression of the LSM14B
383 standard isoform was dramatically decreased by 86%(Fig. 8D), whereas expression of
384 the longer isoform was increased by 145% in GV-stage oocytes in *Esrp1*- knockout
385 oocytes (Fig. 8E). Taken together, these data suggest that the global ESRP1-mediated
386 AS program was required for maintaining spindle morphogenesis and oocyte meiosis.
387

388 **Discussion**

389 Our present study represents the first report to show that the splicing factor, ESRP1,
390 controls oocyte meiosis and follicular development via pre-mRNA splicing in mice.
391 We found that an abnormal splicing program resulting from ESRP1 deletion induced
392 severe spindle organization defects, chromosome misalignment, abnormal SAC
393 activation, and insufficient APC/C activity. These defects collectively resulted in
394 first-meiosis arrest (Fig. 9). Since ESRP1 deletion hampered follicular development
395 and ovulation, female infertility and ultimate POF were found in *Esrp1*-knockout

396 mice.

397 Post-transcriptional modifications of mRNAs via AS are particularly critical in
398 oocytes, as oocyte maturation is associated with suppression of transcription, and new
399 mRNAs are not synthesized until after zygotic genome activation (ZGA) that occurs
400 at the two-cell stage in mice (Flach et al. 1982). Gene transcription in the one- cell
401 stage is uncoupled with splicing and 3' processing, leaving most transcripts
402 nonfunctional and genes transcribed in zygotes yield functional mRNAs until two-
403 cell stage (Abe et al. 2015). During the period from oocyte maturation to ZGA, gene
404 expression is mainly mediated by regulation of maternal mRNAs accumulated in the
405 oocyte prior to meiotic reactivation (Christou-Kent et al. 2020; Sha et al. 2020).

406 ESRP1 is an RBP that regulates AS and has been found to be universally
407 expressed in organisms that have been analyzed. Warzecha et al showed that ESRP1
408 binds to the *Fgfr2* auxiliary cis-element, intronic splicing enhancer/intronic splicing
409 silencer-3 (ISE/ISS-3), to regulate splicing that is required for the expression of
410 epithelial *Fgfr2*-IIIb. ISE/ISS-3 is located in the intron between mutually exclusive
411 exons IIIb and IIIc, and ESRP1 promotes splicing of the upstream exon IIIb while
412 silencing the downstream exon IIIc (Warzecha et al. 2009a). In our present study,
413 mutually exclusive exons of *Fgfr2* were also found from our single-cell RNA-Seq
414 data, consistent with the conventional action of ESRP1 in promoting exon inclusion
415 by binding downstream of a regulated exon and possibly acting as an exon-skipping
416 enhancer by binding to upstream introns (Warzecha et al. 2010). AS deficiency
417 caused by ESRP1 has been reported in several mouse organs. ESRP1 enhances the
418 expression of CD44v in breast cancer cells through AS, promoting breast cancer to
419 lung metastasis and colonization independently of EMT (Yae et al. 2012); moreover,
420 ablation of *Esrp1* results in ureteric branching defects and reduces nephron number
421 due to incorrect *Fgfr2* splicing (Bebee et al. 2016). In the present study, ESRP1 was
422 expressed in oocytes at all follicular stages. Since we found that ESRP1 was
423 preferentially localized to the nucleus with active transcription at the NSN-GV stage,

424 we investigated the function of ESRP1 during oocyte development and maturation in
425 mice. Single-cell RNA-Seq analysis of *Esrp1*- knockout oocytes showed that ESRP1
426 determined the pre-mRNA processing of the oocyte maternal transcriptome. Thus,
427 *Esrp1*$^{fl/fl}$/*Gdf9-Cre* mice represent a model for investigating AS related to mouse
428 meiosis. Previous work has shown that BCAS2 is involved in pre-mRNA splicing in
429 spermatogonia in mouse testes. Disruption of *Bcas2* leads to a significant shift of
430 isoforms of DAZL protein and impairs spermatogenesis and male mouse fertility (Liu
431 et al. 2017). However, few studies have investigated the role of AS in female
432 germ-cell development. Here, we revealed that ESRP1 mediated critical roles of the
433 pre-mRNA splicing program necessary for female mouse fertility.

434 In the present study, ESRP1 deletion led to oocyte arrest at metaphase I, with
435 abnormal spindle organization. In mouse oocytes, homologous chromosome
436 separation requires separase to cleave the meiotic kleisin, REC8, and this step
437 depends on APC/C-mediated degradation of cyclin B1 and securin (Herbert et al.
438 2003; Kudo et al. 2006). Furthermore, timely APC/C activation depends on
439 satisfaction of the SAC (Holt et al. 2013; Touati and Wassmann 2016). In the present
440 study, in *Esrp1*- knockout oocytes, defects in spindle organization and the presence of
441 unattached chromosomes triggered SAC activity (Touati et al. 2015) and may have
442 led to insufficient APC/C activity. Inhibition of SAC activity could partially rescue
443 metaphase I arrest caused by *Esrp1* deficiency. Both activated SAC and insufficient
444 APC/C activity may lead to metaphase-I arrest and affect the expression of numerous
445 oocyte meiosis-related genes such as *Marf1* (Su et al. 2012).

446 Nevertheless, our present study showed that ESRP1 played pivotal roles in
447 spindle/chromosome organization in mouse oocytes through AS. Maternal *Esrp1*
448 depletion affects splicing of several hundred genes. Following these alterations in
449 splicing, microtubule cytoskeletal organization was the most significantly affected
450 process, and many ESRP1-controlled genes were associated with spindle organization.
451 Mitotic kinesin-like protein 1 (MKlp1, also known as *Kif23*) contributes to the

452 shortening and widening of the spindle during metaphase-I arrest in drosophila
453 oocytes, and a partial depletion of MKlp1 produces significantly longer and narrower
454 spindles in oocytes (Costa and Ohkura 2019). Tumor suppressor p53 binding protein
455 1 (*Trp53bp1*) plays a role in maintaining the bipolar spindle during mitosis (Lambrus
456 et al. 2016). Recent studies have revealed that *Trp53bp1* knockdown affects spindle
457 bipolarity and chromatin alignment by altering MTOC stability during oocyte
458 maturation (Jin et al. 2019). In our present study, we also found abnormal splicing of
459 *Rac1*, which has previously been shown to contribute to spindle positioning and
460 oocyte cortical polarity during mouse oocyte meiosis (Halet and Carroll 2007).
461 CENP-A, a variant of histone H3 specific for nucleosomes at centromeres, is required
462 for the localization of all known kinetochore components. Preventing CENP-A
463 deposition during prophase I-arrested oocytes results in a failure of kinetochore
464 function, perturbs chromosome segregation, and ultimately cell dysfunction(Swartz et
465 al. 2019). Mitotic centromere associated kinesin (MCAK; also known as *Kif2c*) is an
466 important regulator of microtubule dynamics in a variety of systems, and knockdown
467 of MCAK causes a delay in chromosome congression and induces a meiosis I arrest in
468 mouse oocytes (Illingworth et al. 2010; Vogt et al. 2010). BORA is a critical regulator
469 of Aurora A and Plk1, and a partial depletion of *Bora* affects mouse oocyte
470 maturation and caused MI-arrest with spindle/chromosome disorganization and the
471 disappearance of Aurora A and Plk1 at the spindle in oocytes(Zhai et al. 2013).
472 Neurodevelopment protein 1-like 1 (*Ndel1*, also known as *NudEL*), is a dynein
473 accessory protein. *Ndel1* mutant impairs the dynein-mediated transport of kinetochore
474 proteins to spindle poles along microtubules, a process contributing to inactivation of
475 the SAC in mitosis (Yan et al. 2003). KIF3A is involved in chromosomal structure
476 maintenance (Monzo et al. 2012). Thus, a comprehensive set of abnormalities in
477 splicing patterns of important genes regulated by ESRP1 may contribute to mouse
478 meiotic arrest and infertility (Fig. 9).
479 LSM14 belongs to the RNA-associated protein (RAP) family and has been shown

480 to exert roles in both mRNA storage and posttranscriptional regulation. Recent studies
481 have shown that knockdown of LSM14B induces oocyte metaphase-I arrest and
482 misalignment of chromosomes due to abnormal activation of SAC and MPF (Zhang et
483 al. 2017). In the present study, from our single-cell sequencing data, we observed that
484 the sixth exon of *Lsm14b* was spliced in *Esrp1*$^{fl/fl}$ oocytes but was retained in *Esrp1*-
485 knockout oocytes. Considering the profound effect of *Esrp1* loss on oocyte meiosis,
486 the corresponding dramatic changes in *Lsm14b* have attracted particular interest. Here,
487 we found that the protein level of the standard isoform of LSM14B was dramatically
488 reduced, while the longer isoform of LSM14B was significantly up-regulated in
489 GV-stage and ovulated oocytes from *Esrp1*$^{fl/fl}$*/Gdf9-Cre* mice (Fig. 8C, D, E),
490 suggesting that the standard isoform of LSM14B might represent the main functional
491 form during mouse meiosis. Deletion of ESRP1 leads to dramatic retention of the
492 sixth exon in LSM14B, suggesting a critical role for the precise control of *Lsm14b*
493 splicing during normal mouse meiosis. However, the normal function of the longer
494 isoform of LSM14B, with retention of the sixth exon, remains unknown. The
495 dramatic decrease in LSM14B standard isoform and total LSM14B protein that we
496 found in the present study suggests that deletion of ESRP1 leads to a significant
497 degree of loss-of-function of LSM14B. In addition, a previous study has shown that
498 LSM14B regulates the oocyte meiotic maturational process by controlling mRNA
499 expression and degradation, such as of *Cyclin B1* and *Cdc20*, which are essential for
500 the cell cycle (Zhang et al. 2017). Consistently, in our present study, we also
501 confirmed that the mRNA levels of *Cyclin B1* and *Cdc20* were downregulated in
502 GV-stage and ovulated oocytes from *Esrp1*$^{fl/fl}$*/Gdf9-Cre* mice. These data suggest that
503 ESRP1 might be critical for mouse meiosis via regulating *Lsm14b* splicing (Fig. 9).
504 Collectively, our present findings seem to mimic the process in which AS defects
505 cause abnormal oocyte meiosis, follicular development and ovulation disorders, and
506 ultimate POF.

507 In summary, our present study is the first to elucidate that the RBP, ESRP1, is
508 required for spindle organization, chromosome segregation during oocyte meiosis,
509 and follicular development. Our findings shed light on the importance of AS in
510 regulating female germline development and fertility and may also provide novel
511 insights toward the clinical prediction of POF.
512

513 **Materials and Methods**

514 **Animals**

515 Mouse colonies in the present study were housed and maintained under
516 specific-pathogen-free conditions in the Animal Core Facility of Nanjing Medical
517 University (China). Mice were housed under a 12/12-h light/dark cycle, and food and
518 water were provided *ad libitum*. All procedures and protocols involving mice were
519 approved by the Institutional Animal Care and Use Committee (IACUC) at Nanjing
520 Medical University (ID: IACUC1812016).

521 **Generation of *Esrp1$^{fl/\triangle}$/Ddx4-Cre and Esrp1$^{fl/fl}$/Gdf9-Cre* mice**

522 The targeting construct contained three *loxP* sites inserted into intron 6 and intron 9 of
523 the *Esrp1* gene and a floxed HyTK double-selection cassette in exons 7–9. All three
524 *loxP* sites were in the same orientation (Fig. S2A). The *Ddx4-Cre* (*Vasa-Cre*) mouse
525 line was maintained on a mixed genetic background (129/C57BL/6×FVB/N) (cat.
526 #J006954, Jackson Laboratory, Bar Harbor, ME). The Tg(Gdf9-iCre)5092Coo mouse
527 line was maintained on the C57BL/6J genetic background (cat. #J011062, Jackson
528 Laboratory). *Esrp1$^{fl/fl}$* mice were crossed with *Ddx4-Cre/+* or *Gdf9-Cre/+* transgenic
529 mice to generate PGCs-specific *Esrp1*-knockout (*Esrp1$^{fl/\triangle}$/Ddx4-Cre)* mice or
530 oocyte-specific *Esrp1*-knockout (*Esrp1$^{fl/fl}$ /Gdf9-Cre*) mice, respectively. Offspring
531 was genotyped by PCR using specific primers (Table S1).

532 **Fertility analysis**

533 For fertility assessment of *Esrp1$^{fl/\triangle}$/Ddx4-Cre* mice, 8-week-old *Esrp1$^{fl/fl}$* (control; n
534 =6) and *Esrp1$^{fl/\triangle}$/Ddx4-Cre* mice (n = 6) were separately mated with WT C57BL/6

535 mice respectively at a ratio of 1:1. For *Esrp1*$^{fl/fl}$ */Gdf9-Cre* mice, 8-week-old females
536 (n = 6) were separately mated with WT C57BL/6 males at a ratio of 1:1. Mating pairs
537 were continuously housed together for a period of six months, parturition frequency
538 and litter sizes were assessed.

539 **Superovulation, oocyte collection, fertilization, and embryo culture**

540 Most mice, unless specify, used in this study were 4-6-week-old. For the
541 superovulation assay, mice were intraperitoneally injected with 5 international units
542 (IU) of PMSG (lot. #190915, Ningbo Sansheng Pharmaceutical, CHN) to stimulate
543 antral follicular development and 44– 46 h later with another 5 IU of hCG (lot.
544 #180428, Ningbo Sansheng Pharmaceutical, CHN), 14–16 h later, cumulus-oocyte
545 complexes (COCs) were surgically disassociated from oviducts and digested with
546 0.5mg/ml hyaluronidase (cat. #H4272, Sigma-Aldrich, USA), and the total ovulated
547 oocyte number was counted. For oocyte collection, mice were prepared by
548 intraperitoneal injection of 5 IU of PMSG 44– 46 h before oocyte collection.
549 Fully-grown oocytes arrested at germinal vesicle (GV) stage were collected from
550 ovaries in M2 medium (Cat. #M7167, Sigma-Aldrich) with 5 μM Milrinone (Cat.
551 #475840, Millipore, USA). Cumulus cells were removed by gently pipetting. For
552 IVM, oocytes with the intact GV were selected for culture in the M2 medium under
553 paraffin oil at 37°C in a 5% CO_2 atmosphere. Cells were removed from culture at the
554 appropriate stages or time points for the following assays. The progress of meiosis in
555 the oocytes was determined based on the ratio of GVBD and PBE. For Mps1
556 inhibition, reversine (cat. #10004412, Cayman Chemical Research) was added to the
557 culture medium 5.5 h after GVBD at a final concentration of 0.5 μM. As oocytes are
558 cultured in drops covered with mineral oil and because reversine is soluble in oil,
559 mineral oil covering the culture drops contained reversine as well, and untreated
560 controls were cultured in separate dishes. For IVF, normal sperm isolated from
561 B6D2F1 adult males were inseminated with the ovulated oocytes with visible PB1 or
562 COCs. Formation of 2-cell stage embryos was scored 24 h after IVF, and 2-cell stage

563 embryos were transferred into KSOM (cat. #MR-020P-5F, Millipore, USA) medium
564 for further development. Development of 2-cell embryos to the blastocyst stage was
565 scored 3–5 days after culture. Oocytes and embryos morphology were observed and
566 images were acquired with a stereoscope (1X51/0N3-M300, Olympus, Germany).
567 **Histology, immunofluorescence, and immunohistochemistry**
568 Tissues were fixed in Modified Davidson's Fluid (MDF) overnight at room
569 temperature and were then embedded in either paraffin—for histological and
570 immunohistochemical analyses—or in 4% paraformaldehyde (PFA, cat. #P6148,
571 Sigma-Aldrich) overnight at 4°C, after which tissues were embedded in
572 optimal-cutting-temperature compound (OCT, cat. #4583, Sakura) for
573 immunofluorescence. Paraffin sections (5 μm) were stained with hematoxylin and
574 eosin (HE) and observed under a microscope (Axio Scope A1, Carl Zeiss, Germany).
575 Follicles at different developmental stages were counted in every third section
576 throughout the whole ovary. To avoid repeated counting of the same follicle, only
577 follicles containing an oocyte with visible GV were counted. The stages of follicles
578 were categorized as follows: primordial follicles were surrounded by a layer of
579 partially or intact squamous granules; primary follicles were surrounded by a layer of
580 cuboidal granulosa cells; early-secondary follicles had less than or equal to two layers
581 of granulosa cells; later-secondary follicles had more than two layers of granulosa
582 cells without visible antrum; and antral follicles had fluid-filled antrum forms. For
583 immunofluorescence and immunohistochemistry, following hydration and antigen
584 retrieval, tissue sections (5 μm) were permeated in PBS containing 0.3% Triton X-100
585 for 15 min, blocked with 3% bovine serum albumin (BSA, cat. #A3803,
586 Sigma-Aldrich) in PBS for 2 h at room temperature, and were incubated with primary
587 antibodies (Table S2) diluted in 3% BSA overnight at 4°C. After washing three times
588 with PBS, sections were incubated with TRITC/FITC-conjugated secondary antibody
589 (Table S2) for immunofluorescence or with horseradish peroxidase (HRP)-conjugated
590 secondary antibody (Table S2) and diaminobenzidine (DAB, cat. #ZLI9017,

591 Zhongshan Jinqiao biotechnology) for immunohistochemistry. The sections were then
592 washed with PBS three times, incubated with DAPI (1μg/ml in PBS, cat. #D9542,
593 Sigma-Aldrich) for 10 min at room temperature, and observed using a confocal
594 laser-scanning microscope (LSM 800, Carl Zeiss, Germany) or ZEISS Axio Scope A1.
595 For oocytes immunofluorescence, oocytes were fixed in 4% PFA for 30 min at room
596 temperature, permeated in PBS containing 0.5% Triton X-100 for 20 min at room
597 temperature, blocked with 1% BSA in PBS for 1 h at room temperature and were
598 incubated with the primary antibody (Table S2) overnight at 4°C. Following washing
599 three times with PBST (0.1% Tween 20 and 0.01% Triton X-100 in PBS), oocytes
600 were incubated with appropriate secondary antibody (Table S2) for 1 h at room
601 temperature. After washing three times, oocytes were stained with DAPI (1μg/ml in
602 PBS) for 10 min. For K-MT attachments assessment, oocytes were briefly chilled at
603 4°C to induce depolymerization of non-kinetochore microtubules just prior to fixation.
604 Finally, oocytes were mounted on slides in an anti-fade reagent (cat. #P0126,
605 Beyotime, CHN), and observed using a confocal laser-scanning microscope (LSM
606 800, Carl Zeiss, Germany).

607 **5-Ethynyl uridine (EU) staining**

608 The 5-ethynyl uridine (5-EU) staining was performed with a Cell-Light EU
609 Apollo567 RNA Imaging Kit (cat. #C00031, RiboBio, CHN) according to the
610 manufacturer's instructions, with the exception that 5-EU was added to the M2
611 medium with 5 μM of milrinone and was incubated with GV oocytes for 2 h.
612 Subsequently, immunofluorescence was performed as described above.

613 **Single-cell RNA sequencing**

614 A total of eight oocyte RNA samples were used from six-week-old *Esrp1*$^{fl/fl}$ and
615 *Esrp1*$^{fl/fl}$*/Gdf9-Cre* female mice according to four individual collections. One in every
616 15 oocytes was collected in a tube with ribonuclease inhibitor (cat. #Y9240L,
617 Enzymatics, GER) and lysis buffer. The directly lysed oocytes were used for cDNA
618 synthesis using Smart-seq2. After amplification, the cDNA was fragmented by

619 ultrasonic waves using a Bioruptor Sonication System (Diagenode Inc., Denville,
620 USA). Sequencing libraries were made with the fragmented DNA using a NEBNext
621 Ultra DNA Library Prep Kit for Illumina according to the manufacturer's instructions
622 (cat. #E7370, New England Biolabs, USA). Library quality inspection was established
623 via a LabChip GX Touch (PerkinElmer) and Step OnePlus Real-Time PCR System
624 (ThermoFisher, USA). Qualified libraries were then loaded on a HiSeq X Ten
625 platform (Illumina, San Diego, USA) for paired-end 150-bp sequencing.

626 **RNA extraction and reverse-transcription PCR (RT-PCR)**

627 Total RNA was extracted using RNeasy Micro Kits (cat. #74004, Qiagen, GER)
628 according to the manufacturer's instructions. Reverse transcription (RT) was
629 performed using the PrimeScript RT master mix (cat. #RR036A, Takara, Japan).
630 Real-time RT-PCR was performed in a StepOne plus system (ABI StepOne Plus,
631 ThermoFisher, USA) using SYBR green master mix (cat. #Q141-02, Vazyme, China).
632 Threshold cycle (*Ct*) values were obtained, and the *ΔΔCt* method was used to
633 calculate the fold changes. All of the values were normalized to 18s. Primer
634 sequences are listed in Table S1.

635 **Protein extraction and western blot**

636 Oocytes were collected from *Esrp1*$^{fl/fl}$ and *Esrp1*$^{fl/fl}$ */Gdf9-Cre* female at indicated time
637 points, and washed in PBS-PVA to remove proteins from the medium. All samples
638 were lysed in RIPA buffer (cat. #P0013C, Beyotime, CHN) containing protease
639 inhibitor cocktail (cat. #11697498001, Roche, USA). The samples were loaded into
640 5×SDS loading buffer (cat. #P0015L, Beyotime, CHN) and boiled for 5 min. The
641 lysates were subjected to 5% Sodium dodecyl sulfate polyacrylamide gel
642 electrophoresis (SDS-PAGE) stacking gel at 80 V and a 10% SDS-PAGE separating
643 gel at 120 V. The separated proteins were transferred onto polyvinylidene fluoride
644 (PVDF) membranes (cat. #162-0177, Bio-Rad, USA). Thereafter, membranes were
645 blocked in 5% skimmed milk in TBST (Tris buffered saline containing 0.1%
646 Tween-20) for 2 h at room temperature and incubated with primary antibody (Table

647 S2) overnight at 4°C. After washing with TBST three times, the membranes were
648 incubated with a secondary antibody conjugated with HRP (Table S2) for 2h at room
649 temperature, followed by stringent washing. Protein bands were detected by using
650 ECL reagent (NEL105001EA, Perkinelmer, USA).

651 **Chromosome spreads**

652 For chromosome spreads, oocytes were harvested from *Esrp1*$^{fl/fl}$ and *Esrp1*$^{fl/fl}$
653 */Gdf9-Cre* female. Oocytes were exposed to acid Tyrode's solution (cat. #T1788,
654 Sigma-Aldrich, USA) for 1-2 min at 37 °C to remove zona pellucidae. Next, the
655 oocytes were recovered in M2 medium for 10 min, and fixed in a drop of spread
656 solution with 1% PFA, 0.15% Triton X-100, and 3mM DTT (cat. #R0861, Thermo
657 Scientific, USA) on the clean glass slides. After air-drying, the slides were blocked
658 with 1% BSA in PBS for 1h at room temperature and incubated with the primary
659 antibody (Table S2) overnight at 4°C, then incubated with corresponding secondary
660 antibodies (Table S2) for 1 h at at room temperature. DNA counterstaining were
661 stained with DAPI (1μg/ml in PBS) and observed using a confocal laser-scanning
662 microscope (LSM 800, Carl Zeiss, Germany).

663 **Statistical analysis**

664 All experiments were performed at least three times independently. All quantitative
665 data are presented as the mean ± the standard error of mean (SEM), and analyses were
666 carried out via GraphPad Prism 8.00 (GraphPad Software, Inc.). Statistical differences
667 between each group were analyzed by two-tailed Student's *t* tests or rank-sum tests
668 via SPSS software 19.0 (IBM Corporation). A P value < 0.05 was considered to be
669 statistically significant.

670 **Data availability**

671 RNA sequencing data reported in this paper are accessible through the NCBI Gene
672 Expression Omnibus (GEO) accession number GSE149355.

673

674

675 **Acknowledgments**

676 We would like to thank CAM-SU International Cooperation Center, Soochow
677 University, China for help in generation of *Esrp1-floxed* mice. We are grateful to all
678 female fertility research groups (Dr YQ Su, J Li, Q Wang and D Zhang) at SKLRM
679 for their valuable comments and technical help. We thank to Dr Ralph L Brinster for
680 his support on the finding of RBP profiling in germline cells (Dr Xin Wu was a
681 previous postdoc from Brinster lab) and Dr Jeremy P Wang at University of
682 Pennsylvania for the suggestion and support for the RBP studies (Dr Jian Zhou is a
683 previous postdoc from Wang lab). We thanks to LetPub for help with manuscript
684 grammar checking. We also thank all valuable helps from the members in Wu
685 laboratory. The work was supported by the National Key R&D Program of China
686 (2018YFC1003302 to XW), the National Natural Science Foundation of China
687 (31872844 to XW), the National Natural Science Foundation of Jiangsu Province
688 (BK20181134 to JZ).

689 **Author contributions**

690 X.W and J.Z conceived the study. L.P.Y., X.B.G., and H.R.Z. bred the mice. L.P.Y.,
691 and H.R.Z. performed most of the experiments, J.Z. constructed the ES cell targeting.
692 L.P.Y., and D.D.Q. designed the primers to verify the aberrant splicing patterns.
693 L.P.Y. prepared the figures. L.P.Y. and X.W wrote the manuscript. The manuscript
694 was reviewed by all authors.

695

696 **Reference**

697 Abe K, Yamamoto R, Franke V, Cao M, Suzuki Y, Suzuki MG, Vlahovicek K,
698 Svoboda P, Schultz RM, Aoki F. 2015. The first murine zygotic transcription
699 is promiscuous and uncoupled from splicing and 3' processing. *The EMBO*
700 *journal* **34**: 1523-1537.
701 Bebee TW, Park JW, Sheridan KI, Warzecha CC, Cieply BW, Rohacek AM, Xing Y,
702 Carstens RP. 2015. The splicing regulators Esrp1 and Esrp2 direct an
703 epithelial splicing program essential for mammalian development. *eLife* **4**.
704 Bebee TW, Sims-Lucas S, Park JW, Bushnell D, Cieply B, Xing Y, Bates CM,
705 Carstens RP. 2016. Ablation of the epithelial-specific splicing factor Esrp1

706 results in ureteric branching defects and reduced nephron number.
707 *Developmental dynamics : an official publication of the American Association*
708 *of Anatomists* **245**: 991-1000.
709 Bennabi I, Terret ME, Verlhac MH. 2016. Meiotic spindle assembly and chromosome
710 segregation in oocytes. *J Cell Biol* **215**: 611-619.
711 Black DL. 2000. Protein diversity from alternative splicing: a challenge for
712 bioinformatics and post-genome biology. *Cell* **103**: 367-370.
713 Brown RL, Reinke LM, Damerow MS, Perez D, Chodosh LA, Yang J, Cheng C.
714 2011. CD44 splice isoform switching in human and mouse epithelium is
715 essential for epithelial-mesenchymal transition and breast cancer progression.
716 *The Journal of clinical investigation* **121**: 1064-1074.
717 Christou-Kent M, Dhellemmes M, Lambert E, Ray PF, Arnoult C. 2020. Diversity of
718 RNA-Binding Proteins Modulating Post-Transcriptional Regulation of Protein
719 Expression in the Maturing Mammalian Oocyte. *Cells* **9**.
720 Costa MFA, Ohkura H. 2019. The molecular architecture of the meiotic spindle is
721 remodeled during metaphase arrest in oocytes. *J Cell Biol* **218**: 2854-2864.
722 Do DV, Strauss B, Cukuroglu E, Macaulay I, Wee KB, Hu TX, Igor RLM, Lee C,
723 Harrison A, Butler R et al. 2018. SRSF3 maintains transcriptome integrity in
724 oocytes by regulation of alternative splicing and transposable elements. *Cell*
725 *discovery* **4**: 33.
726 Du G, Wang X, Luo M, Xu W, Zhou T, Wang M, Yu L, Li L, Cai L, Wang PJ et al.
727 2020. mRBPome capture identifies the RNA-binding protein TRIM71, an
728 essential regulator of spermatogonial differentiation. *Development*
729 *(Cambridge, England)* **147**.
730 Flach G, Johnson MH, Braude PR, Taylor RA, Bolton VN. 1982. The transition from
731 maternal to embryonic control in the 2-cell mouse embryo. *The EMBO journal*
732 **1**: 681-686.
733 Graveley BR, Brooks AN, Carlson JW, Duff MO, Landolin JM, Yang L, Artieri CG,
734 van Baren MJ, Boley N, Booth BW et al. 2011. The developmental
735 transcriptome of Drosophila melanogaster. *Nature* **471**: 473-479.
736 Halet G, Carroll J. 2007. Rac activity is polarized and regulates meiotic spindle
737 stability and anchoring in mammalian oocytes. *Dev Cell* **12**: 309-317.
738 Hentze MW, Castello A, Schwarzl T, Preiss T. 2018. A brave new world of
739 RNA-binding proteins. *Nat Rev Mol Cell Biol* **19**: 327-341.
740 Herbert M, Levasseur M, Homer H, Yallop K, Murdoch A, McDougall A. 2003.
741 Homologue disjunction in mouse oocytes requires proteolysis of securin and
742 cyclin B1. *Nat Cell Biol* **5**: 1023-1025.
743 Hodges CA, Hunt PA. 2002. Simultaneous analysis of chromosomes and
744 chromosome-associated proteins in mammalian oocytes and embryos.
745 *Chromosoma* **111**: 165-169.
746 Holt JE, Lane SI, Jones KT. 2013. The control of meiotic maturation in mammalian
747 oocytes. *Current topics in developmental biology* **102**: 207-226.

748 Illingworth C, Pirmadjid N, Serhal P, Howe K, Fitzharris G. 2010. MCAK regulates
749 chromosome alignment but is not necessary for preventing aneuploidy in
750 mouse oocyte meiosis I. *Development (Cambridge, England)* **137**: 2133-2138.
751 Jin ZL, Suk N, Kim NH. 2019. TP53BP1 regulates chromosome alignment and
752 spindle bipolarity in mouse oocytes. *Molecular reproduction and development*
753 **86**: 1126-1137.
754 Kageyama S, Liu H, Kaneko N, Ooga M, Nagata M, Aoki F. 2007. Alterations in
755 epigenetic modifications during oocyte growth in mice. *Reproduction* **133**:
756 85-94.
757 Kasowitz SD, Ma J, Anderson SJ, Leu NA, Xu Y, Gregory BD, Schultz RM, Wang
758 PJ. 2018. Nuclear m6A reader YTHDC1 regulates alternative polyadenylation
759 and splicing during mouse oocyte development. *PLoS genetics* **14**: e1007412.
760 Kudo NR, Wassmann K, Anger M, Schuh M, Wirth KG, Xu H, Helmhart W, Kudo H,
761 McKay M, Maro B et al. 2006. Resolution of chiasmata in oocytes requires
762 separase-mediated proteolysis. *Cell* **126**: 135-146.
763 Lambrus BG, Daggubati V, Uetake Y, Scott PM, Clutario KM, Sluder G, Holland AJ.
764 2016. A USP28-53BP1-p53-p21 signaling axis arrests growth after
765 centrosome loss or prolonged mitosis. *J Cell Biol* **214**: 143-153.
766 Lan ZJ, Xu X, Cooney AJ. 2004. Differential oocyte-specific expression of Cre
767 recombinase activity in GDF-9-iCre, Zp3cre, and Msx2Cre transgenic mice.
768 *Biol Reprod* **71**: 1469-1474.
769 Liu W, Wang F, Xu Q, Shi J, Zhang X, Lu X, Zhao ZA, Gao Z, Ma H, Duan E et al.
770 2017. BCAS2 is involved in alternative mRNA splicing in spermatogonia and
771 the transition to meiosis. *Nat Commun* **8**: 14182.
772 Mager LF, Koelzer VH, Stuber R, Thoo L, Keller I, Koeck I, Langenegger M,
773 Simillion C, Pfister SP, Faderl M et al. 2017. The ESRP1-GPR137 axis
774 contributes to intestinal pathogenesis. *eLife* **6**.
775 Mili D, Georgesse D, Kenani A. 2015. Localization and role of RAP55/LSM14 in
776 HeLa cells: a new finding on the mitotic spindle assembly. *Acta Biochim Pol*
777 **62**: 613-619.
778 Monzo C, Haouzi D, Roman K, Assou S, Dechaud H, Hamamah S. 2012. Slow
779 freezing and vitrification differentially modify the gene expression profile of
780 human metaphase II oocytes. *Human reproduction (Oxford, England)* **27**:
781 2160-2168.
782 Nilsen TW, Graveley BR. 2010. Expansion of the eukaryotic proteome by alternative
783 splicing. *Nature* **463**: 457-463.
784 Overlack K, Primorac I, Vleugel M, Krenn V, Maffini S, Hoffmann I, Kops GJ,
785 Musacchio A. 2015. A molecular basis for the differential roles of Bub1 and
786 BubR1 in the spindle assembly checkpoint. *eLife* **4**: e05269.
787 Ramani AK, Calarco JA, Pan Q, Mavandadi S, Wang Y, Nelson AC, Lee LJ, Morris
788 Q, Blencowe BJ, Zhen M et al. 2011. Genome-wide analysis of alternative
789 splicing in Caenorhabditis elegans. *Genome Res* **21**: 342-348.

790 Robinson JT, Thorvaldsdottir H, Winckler W, Guttman M, Lander ES, Getz G,
791 Mesirov JP. 2011. Integrative genomics viewer. *Nature biotechnology* **29**:
792 24-26.
793 Rohacek AM, Bebee TW, Tilton RK, Radens CM, McDermott-Roe C, Peart N, Kaur
794 M, Zaykaner M, Cieply B, Musunuru K et al. 2017. ESRP1 Mutations Cause
795 Hearing Loss due to Defects in Alternative Splicing that Disrupt Cochlear
796 Development. *Dev Cell* **43**: 318-331 e315.
797 Santaguida S, Tighe A, D'Alise AM, Taylor SS, Musacchio A. 2010. Dissecting the
798 role of MPS1 in chromosome biorientation and the spindle checkpoint through
799 the small molecule inhibitor reversine. *J Cell Biol* **190**: 73-87.
800 Sha QQ, Yu JL, Guo JX, Dai XX, Jiang JC, Zhang YL, Yu C, Ji SY, Jiang Y, Zhang
801 SY et al. 2018. CNOT6L couples the selective degradation of maternal
802 transcripts to meiotic cell cycle progression in mouse oocyte. *The EMBO*
803 *journal* **37**.
804 Sha QQ, Zhang J, Fan HY. 2019. A story of birth and death: mRNA translation and
805 clearance at the onset of maternal-to-zygotic transition in mammals†. *Biol*
806 *Reprod* **101**: 579-590.
807 Sha QQ, Zhu YZ, Li S, Jiang Y, Chen L, Sun XH, Shen L, Ou XH, Fan HY. 2020.
808 Characterization of zygotic genome activation-dependent maternal mRNA
809 clearance in mouse. *Nucleic acids research* **48**: 879-894.
810 Su YQ, Sugiura K, Sun F, Pendola JK, Cox GA, Handel MA, Schimenti JC, Eppig JJ.
811 2012. MARF1 regulates essential oogenic processes in mice. *Science (New*
812 *York, NY)* **335**: 1496-1499.
813 Swartz SZ, McKay LS, Su KC, Bury L, Padeganeh A, Maddox PS, Knouse KA,
814 Cheeseman IM. 2019. Quiescent Cells Actively Replenish CENP-A
815 Nucleosomes to Maintain Centromere Identity and Proliferative Potential. *Dev*
816 *Cell* **51**: 35-48.e37.
817 Thornton BR, Toczyski DP. 2003. Securin and B-cyclin/CDK are the only essential
818 targets of the APC. *Nat Cell Biol* **5**: 1090-1094.
819 Touati SA, Buffin E, Cladiere D, Hached K, Rachez C, van Deursen JM, Wassmann
820 K. 2015. Mouse oocytes depend on BubR1 for proper chromosome
821 segregation but not for prophase I arrest. *Nat Commun* **6**: 6946.
822 Touati SA, Wassmann K. 2016. How oocytes try to get it right: spindle checkpoint
823 control in meiosis. *Chromosoma* **125**: 321-335.
824 Vogt E, Sanhaji M, Klein W, Seidel T, Wordeman L, Eichenlaub-Ritter U. 2010.
825 MCAK is present at centromeres, midspindle and chiasmata and involved in
826 silencing of the spindle assembly checkpoint in mammalian oocytes.
827 *Molecular human reproduction* **16**: 665-684.
828 Wang ET, Sandberg R, Luo S, Khrebtukova I, Zhang L, Mayr C, Kingsmore SF,
829 Schroth GP, Burge CB. 2008. Alternative isoform regulation in human tissue
830 transcriptomes. *Nature* **456**: 470-476.
831 Warzecha CC, Jiang P, Amirikian K, Dittmar KA, Lu H, Shen S, Guo W, Xing Y,

832 Carstens RP. 2010. An ESRP-regulated splicing programme is abrogated
833 during the epithelial-mesenchymal transition. *The EMBO journal* **29**:
834 3286-3300.
835 Warzecha CC, Sato TK, Nabet B, Hogenesch JB, Carstens RP. 2009a. ESRP1 and
836 ESRP2 are epithelial cell-type-specific regulators of FGFR2 splicing. *Mol Cell*
837 **33**: 591-601.
838 Warzecha CC, Shen S, Xing Y, Carstens RP. 2009b. The epithelial splicing factors
839 ESRP1 and ESRP2 positively and negatively regulate diverse types of
840 alternative splicing events. *RNA biology* **6**: 546-562.
841 Wu W, Zong J, Wei N, Cheng J, Zhou X, Cheng Y, Chen D, Guo Q, Zhang B, Feng
842 Y. 2018. CASH: a constructing comprehensive splice site method for
843 detecting alternative splicing events. *Brief Bioinform* **19**: 905-917.
844 Yae T, Tsuchihashi K, Ishimoto T, Motohara T, Yoshikawa M, Yoshida GJ, Wada T,
845 Masuko T, Mogushi K, Tanaka H et al. 2012. Alternative splicing of CD44
846 mRNA by ESRP1 enhances lung colonization of metastatic cancer cell. *Nat*
847 *Commun* **3**: 883.
848 Yan X, Li F, Liang Y, Shen Y, Zhao X, Huang Q, Zhu X. 2003. Human Nudel and
849 NudE as regulators of cytoplasmic dynein in poleward protein transport along
850 the mitotic spindle. *Molecular and cellular biology* **23**: 1239-1250.
851 Zhai R, Yuan YF, Zhao Y, Liu XM, Zhen YH, Yang FF, Wang L, Huang CZ, Cao J,
852 Huo LJ. 2013. Bora regulates meiotic spindle assembly and cell cycle during
853 mouse oocyte meiosis. *Molecular reproduction and development* **80**: 474-487.
854 Zhang J, Zhang YL, Zhao LW, Pi SB, Zhang SY, Tong C, Fan HY. 2020. The
855 CRL4-DCAF13 ubiquitin E3 ligase supports oocyte meiotic resumption by
856 targeting PTEN degradation. *Cellular and molecular life sciences : CMLS* **77**:
857 2181-2197.
858 Zhang T, Li Y, Li H, Ma XS, Ouyang YC, Hou Y, Schatten H, Sun QY. 2017.
859 RNA-associated protein LSM family member 14 controls oocyte meiotic
860 maturation through regulating mRNA pools. *The Journal of reproduction and*
861 *development* **63**: 383-388.
862
863
864

865 **Figures and legends**

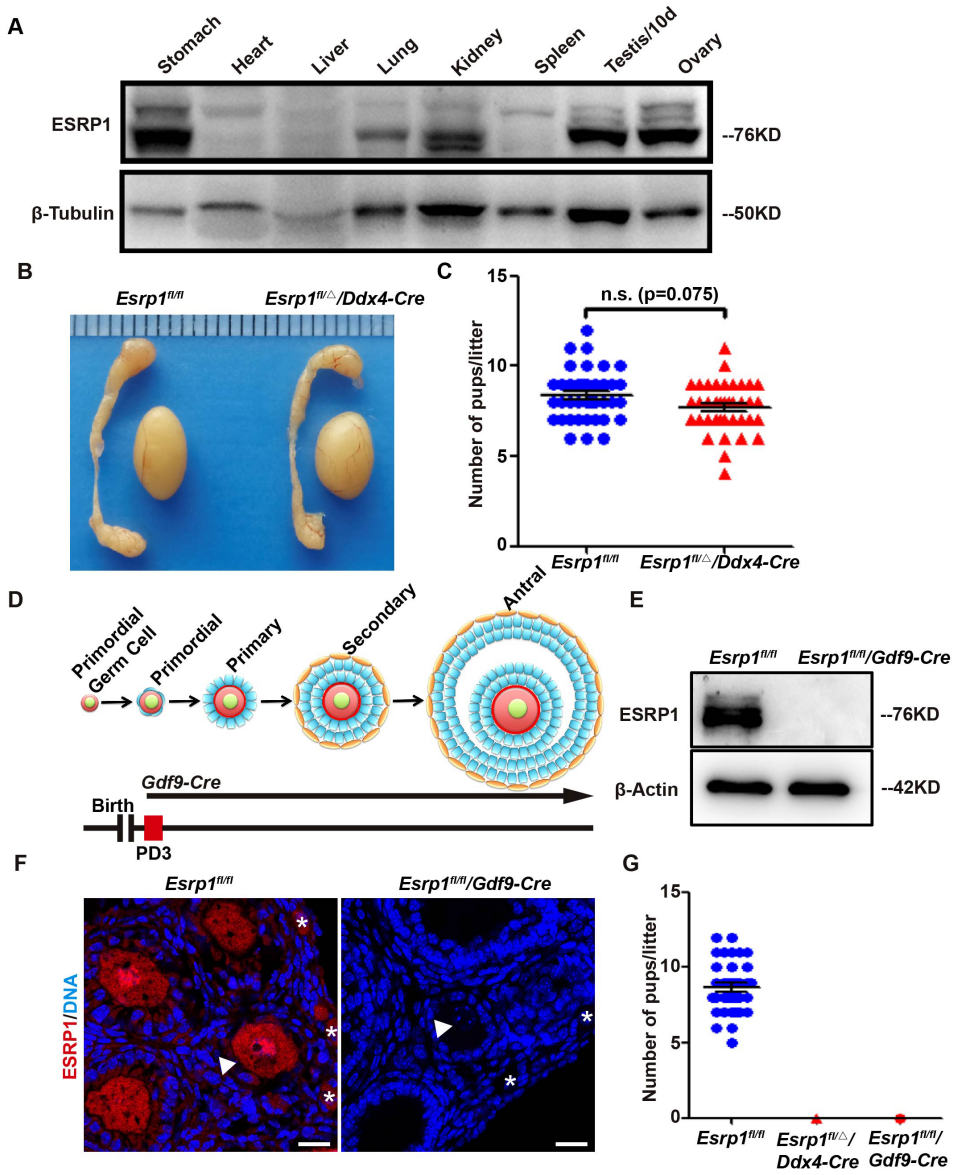

866

867 **Figure 1. Germline deletion of ESRP1 leads to female infertility in mice.** (A)
868 ESRP1 expression in mouse tissues. Western-blot analyses showing the expression of
869 ESRP1 protein in adult mouse stomach, lung, kidney, ovary, and prepubertal
870 testicular tissues. β-tubulin served as a loading control. (B) Morphology of
871 eight-week-old testes and epididymis from *Esrp1*$^{fl/fl}$ and *Esrp1*$^{fl/\triangle}$*/Ddx4-Cre* mice. (C)
872 Fertility analysis of *Esrp1*$^{fl/fl}$ and *Esrp1*$^{fl/\triangle}$*/Ddx4-Cre* males. (D) Schematic diagram of
873 the developmental time point at which *Gdf9-Cre* was expressed. (E) Western-blot
874 analysis showing the expression of ESRP1 protein in GV oocytes from the ovaries of
875 *Esrp1*$^{fl/fl}$ and *Esrp1*$^{fl/fl}$*/Gdf9-Cre* mice. (F) Immunofluorescent staining of ESRP1 (red)

876 in PD21 mouse ovaries. DNA was stained by DAPI (blue). Asterisks indicate oocytes
877 in primordial follicles and white arrowheads point to growing oocytes. Scale bars, 20
878 µm. (G) Fertility analysis of the indicated genotypes mice; *Esrp1*$^{fl/\triangle}$*/Ddx4-Cre* and
879 *Esrp1*$^{fl/fl}$ */Gdf9-Cre* female were infertile.

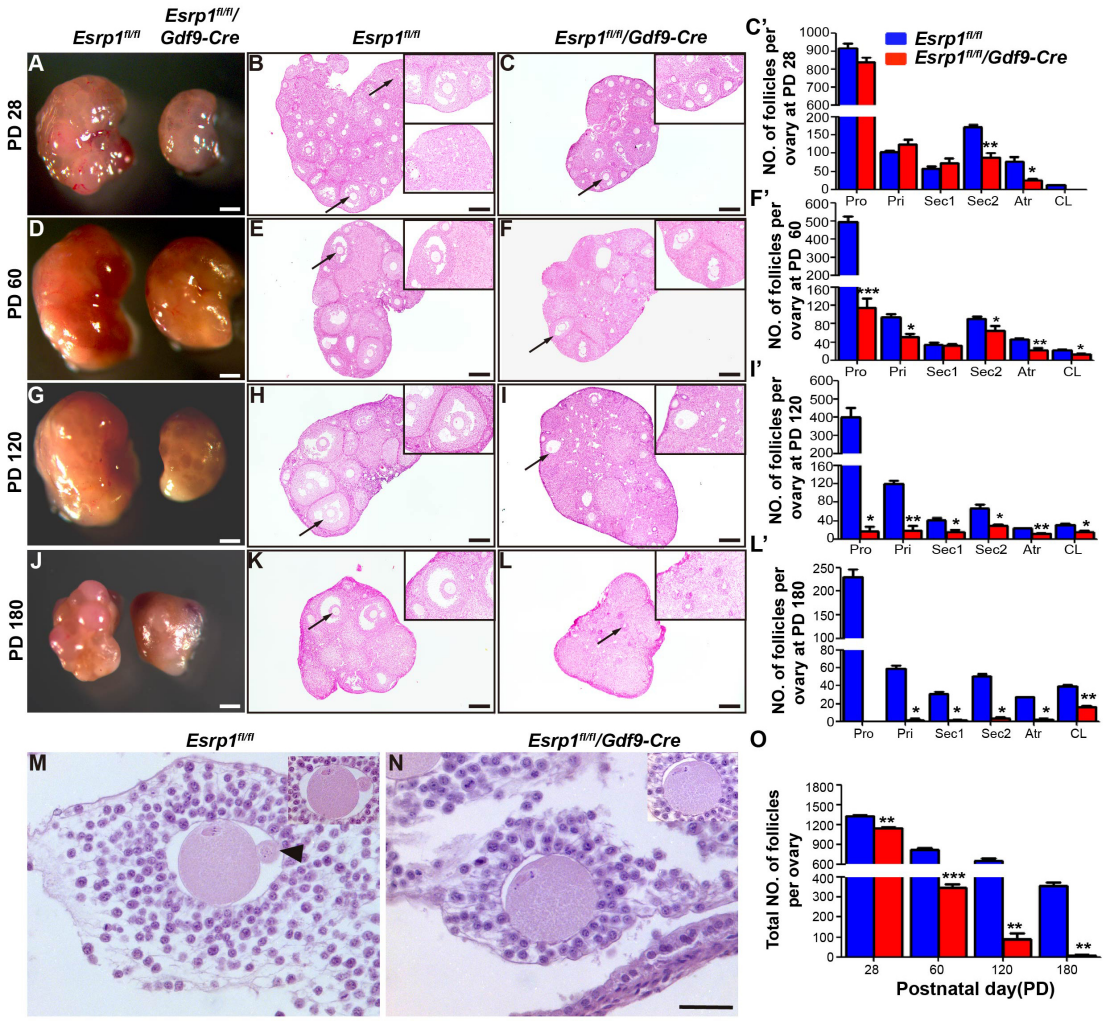

880

881 **Figure 2. ESRP1 is essential for follicular development and oocyte growth.** (A)
882 Morphology of *Esrp1*$^{fl/fl}$ and *Esrp1*$^{fl/fl}$*/Gdf9-Cre* mouse ovaries at PD28. Scale bars,
883 500 µm. (B–C) Hematoxylin/eosin (HE) staining of paraffin slides of ovaries. Arrows
884 and inserts show the antral follicles and corpus luteum at PD28 *Esrp1*$^{fl/fl}$ mice ovaries
885 (B) and antral follicles at PD28 *Esrp1*$^{fl/fl}$ */Gdf9-Cre* ovaries (C). Scale bars, 100 µm.
886 (C') Statistical analysis of the numbers of follicles in the ovaries of *Esrp1*$^{fl/fl}$ (B) and
887 *Esrp1*$^{fl/fl}$*/Gdf9-Cre* (C) mice (*p< 0.05, **p < 0.01). (D) Morphology of *Esrp1*$^{fl/fl}$ and
888 *Esrp1*$^{fl/fl}$*/Gdf9-Cre* mouse ovaries at PD60. Scale bars, 500 µm. (E–F) HE staining

889 showing that the layers of cumulus cells and mural granulosa cells (MGC) of antral
890 follicles at PD60 *Esrp1*$^{fl/fl}$ */Gdf9-Cre* mice ovaries (F, arrow and insert) were
891 significantly thinner compared to those in *Esrp1*$^{fl/fl}$ mice (E, arrow and insert). Scale
892 bars, 100 μm. (F') Statistical analysis of the numbers of follicles in the ovaries of
893 *Esrp1*$^{fl/fl}$ (E) and *Esrp1*$^{fl/fl}$*/Gdf9-Cre* (F) mice (*p< 0.05, **p < 0.01, ***p < 0.001). (G)
894 Morphology of *Esrp1*$^{fl/fl}$ and *Esrp1*$^{fl/fl}$*/Gdf9-Cre* mouse ovaries at PD120. Scale bars,
895 500 μm. (H–I) HE staining showing that the layers of MGC of antral follicles at
896 PD120 *Esrp1*$^{fl/fl}$ */Gdf9-Cre* mice (I, arrow and insert) were significantly thinner
897 compared to those in *Esrp1*$^{fl/fl}$ mice (H, arrow and insert). Scale bars, 100 μm. (I')
898 Statistical analysis of the numbers of follicles in the ovaries of *Esrp1*$^{fl/fl}$ (E) and
899 *Esrp1*$^{fl/fl}$ */Gdf9-Cre* (F) mice (*p< 0.05, **p < 0.01). (J) Morphology of *Esrp1*$^{fl/fl}$ and
900 *Esrp1*$^{fl/fl}$*/Gdf9-Cre* mouse ovaries at PD180. Scale bars, 500 μm. (K–L) HE staining
901 showing that nearly all follicles were absent at PD180 in *Esrp1*$^{fl/fl}$*/Gdf9-Cre* mice (L,
902 arrow and insert) compared to those in *Esrp1*$^{fl/fl}$ mice (K, arrow and insert). Scale bars,
903 100 μm. (L') Statistical analysis of the numbers of follicles in the ovaries of *Esrp1*$^{fl/fl}$
904 (K) and *Esrp1*$^{fl/fl}$*/Gdf9-Cre* (L) mice (*p< 0.05, **p < 0.01). (M–N) Histology of
905 cumulus-oocyte complexes ovulated in oviducts in *Esrp1*$^{fl/fl}$ (M) and
906 *Esrp1*$^{fl/fl}$*/Gdf9-Cre* (N) mice at 16 h after hCG injections. Black arrowheads indicate
907 the first polar body. Scale bars, 100 μm. (O) The total numbers of follicles in *Esrp1*$^{fl/fl}$
908 and *Esrp1*$^{fl/fl}$ */Gdf9-Cre* mice at different ages (*p< 0.05, **p < 0.01, ***p < 0.001).
909 Abbreviations: Pro: primordial follicles; Pri: primary follicles; Sec1: early-secondary;
910 Sec2: later-secondary; Atr: antral follicles; CL: corpus luteum.

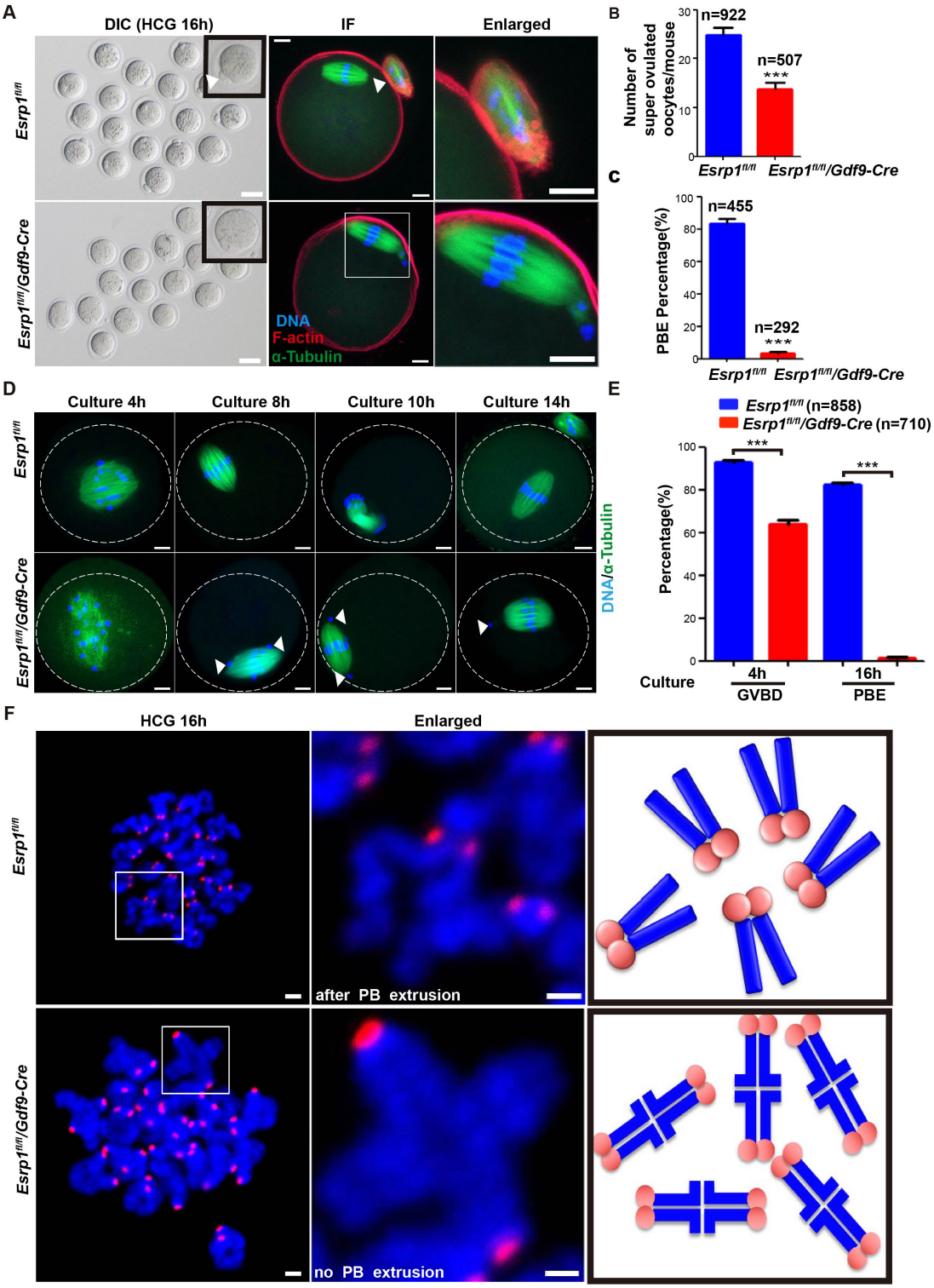

911

912 **Figure 3. ESRP1 is required for the metaphase-to-anaphase-I transition in**

913 **oocytes.** (A) Differential interference contrast (DIC) images of ovulated oocytes from

914 *Esrp1*$^{fl/fl}$ and *Esrp1*$^{fl/fl}$*/Gdf9-Cre* mice at 16 h after hCG injections (left). Scale bars,

915 100 µm. Immunofluorescent staining with α-tubulin (green), F-actin (red), and DAPI

916 (blue) in ovulated oocytes from *Esrp1*$^{fl/fl}$ and *Esrp1*$^{fl/fl}$*/Gdf9-Cre* mice (right). Scale
917 bars, 10 μm. (B) Numbers of oocytes ovulated by *Esrp1*$^{fl/fl}$ mice (24.82 ± 1.47) and
918 *Esrp1*$^{fl/fl}$*/Gdf9-Cre* mice (13.70 ± 1.40) (***P < 0.001). n: number of used oocytes. (C)
919 The rates of MII oocytes with the PB1 from superovulated *Esrp1*$^{fl/fl}$ mice (83.54% ±
920 2.79%) and *Esrp1*$^{fl/fl}$*/Gdf9-Cre* mice (3.10% ± 1.23%) (***P < 0.001). n: number of
921 used oocytes. (D) Immunofluorescent of spindle stained with α-tubulin (green) and
922 chromosomes with DAPI (blue) in oocytes of *Esrp1*$^{fl/fl}$ mice (n=60) and *Esrp1*$^{fl/fl}$
923 */Gdf9-Cre* mice (n=58) at the indicated time points. Dashed lines indicate oocyte
924 outlines, and white arrows indicate lagging chromosomes. Scale bar, 10 mm. (E)
925 GVBD rates of cultured oocytes that were collected at the GV stage from *Esrp1*$^{fl/fl}$
926 mice (92.86% ± 0.89%) and *Esrp1*$^{fl/fl}$*/Gdf9-Cre* mice (64.07% ± 1.56%) (***P <
927 0.001). PBE rates of *Esrp1*$^{fl/fl}$ mice (82.09% ±1.19%) and *Esrp1*$^{fl/fl}$*/Gdf9-Cre* mice
928 (1.10% ± 0.53%) (***P < 0.001). n: number of used oocytes. (F) Chromosome
929 spreads of ovulated oocytes from superovulated *Esrp1*$^{fl/fl}$ and *Esrp1*$^{fl/fl}$ */Gdf9-Cre* mice
930 at 16 h after hCG injections. Kinetochores were stained with CREST (red), and
931 chromosomes were stained with DAPI (blue). The illustrations show typical
932 chromosomes that were observed. Scale bar, 1 μm.

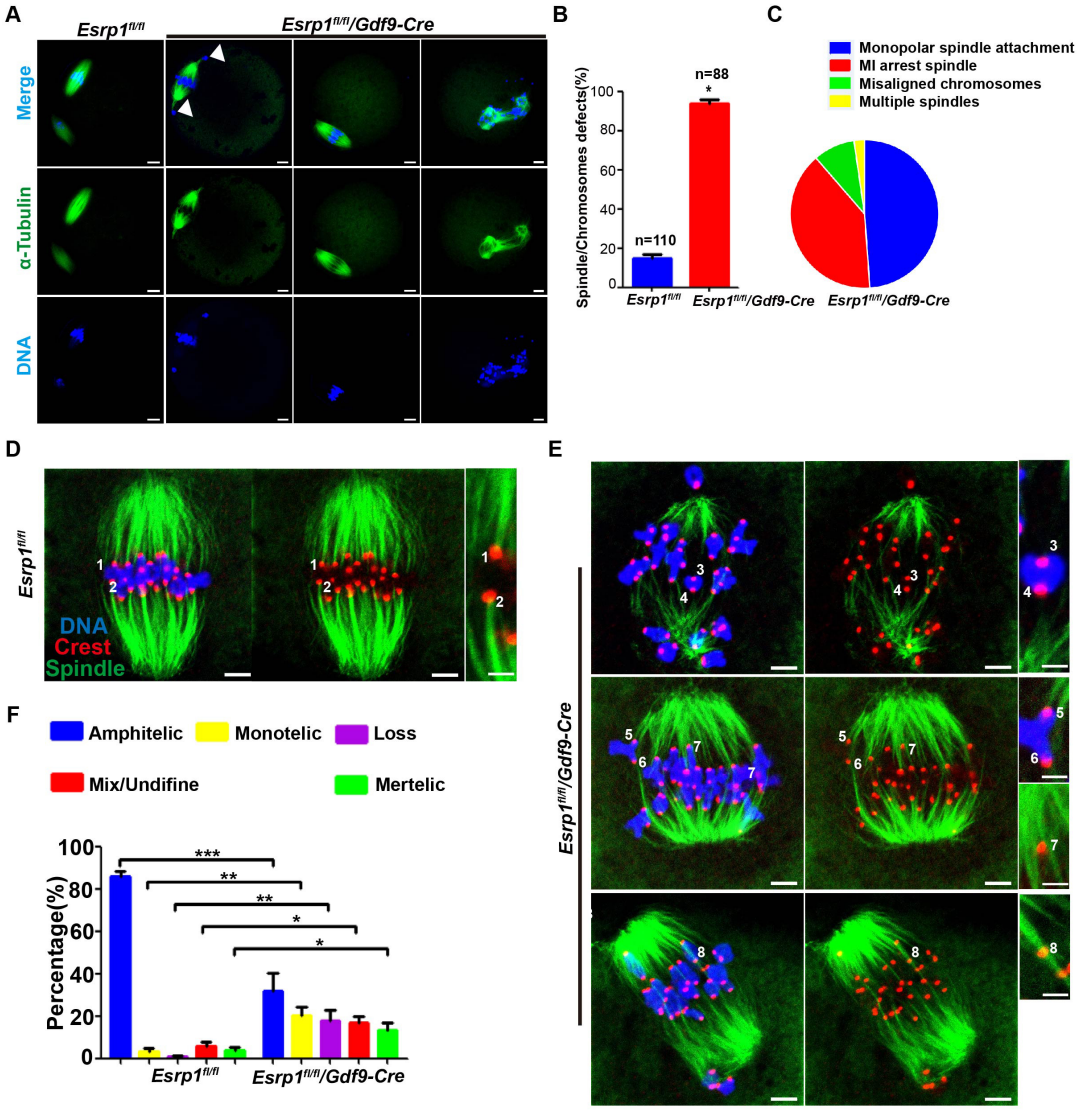

933

934 **Figure 4. *Esrp1* deletion leads to spindle/chromosome disorganization and**

935 **impaired K-MT attachments during oocyte meiosis.**

936 (A) Immunofluorescent staining with α-tubulin to visualize spindles (green) and

937 co-stained with DAPI to visualize chromosomes (blue) in ovulated oocytes of

938 *Esrp1*$^{fl/fl}$ and *Esrp1*$^{fl/fl}$*/Gdf9-Cre* mice. Left, *Esrp1*$^{fl/fl}$ ovulated oocytes presented the

939 PB1, a typical barrel-shaped spindle and well-aligned chromosomes on the metaphase

940 plate; Right, *Esrp1*$^{fl/fl}$*/Gdf9-Cre* ovulated oocytes lacked the PB1, and three examples

941 illustrate apparent monopolar spindle attachments (arrows), metaphase-I arrest

942 spindles, and catastrophic spindle disorganization that were frequently observed in

943 *Esrp1*-knockout oocytes. Representative confocal sections are shown. Scale bar, 10

944 μm. (B) The incidence of abnormal spindles and misaligned chromosomes in *Esrp1*$^{fl/fl}$

945 and *Esrp1*$^{fl/fl}$/*Gdf9-Cre* oocytes (*P < 0.05). n: number of used oocytes. (C) The
946 frequency distribution of *Esrp1*$^{fl/fl}$/*Gdf9-Cre* oocyte phenotypes, within which one
947 oocyte may fall into more than one phenotypic class. (D–E) Control and
948 *Esrp1*-knockout oocytes at MI stage staining with α-tubulin to visualize spindles
949 (green), CREST to detect kinetochore (red), and co-stained with DAPI to visualize
950 chromosomes (blue). (D) Representative confocal image showing the amphitelic
951 attachment in control oocyte (chromosomes 1 and 2). Scale bar, 5 μm or 2 μm. (E)
952 Representative confocal images showing the lost attachment (chromosomes 3 and 4),
953 monotelic attachment (chromosomes 5 and 6), mix/undefined attachment
954 (chromosome 7), as well as merotelic attachment (chromosome 8) in *Esrp1*-knockout
955 oocytes. Scale bar, 5 μm or 2 μm. (F) Quantitative analysis of K-MT attachments in
956 control and *Esrp1*-knockout oocytes. Kinetochores in regions where fibers were not
957 easily visualized were not included in the analysis. 12 control oocytes and 12
958 *Esrp1*-knockout oocytes were examined respectively (*p< 0.05, **p < 0.01, ***p <
959 0.001).

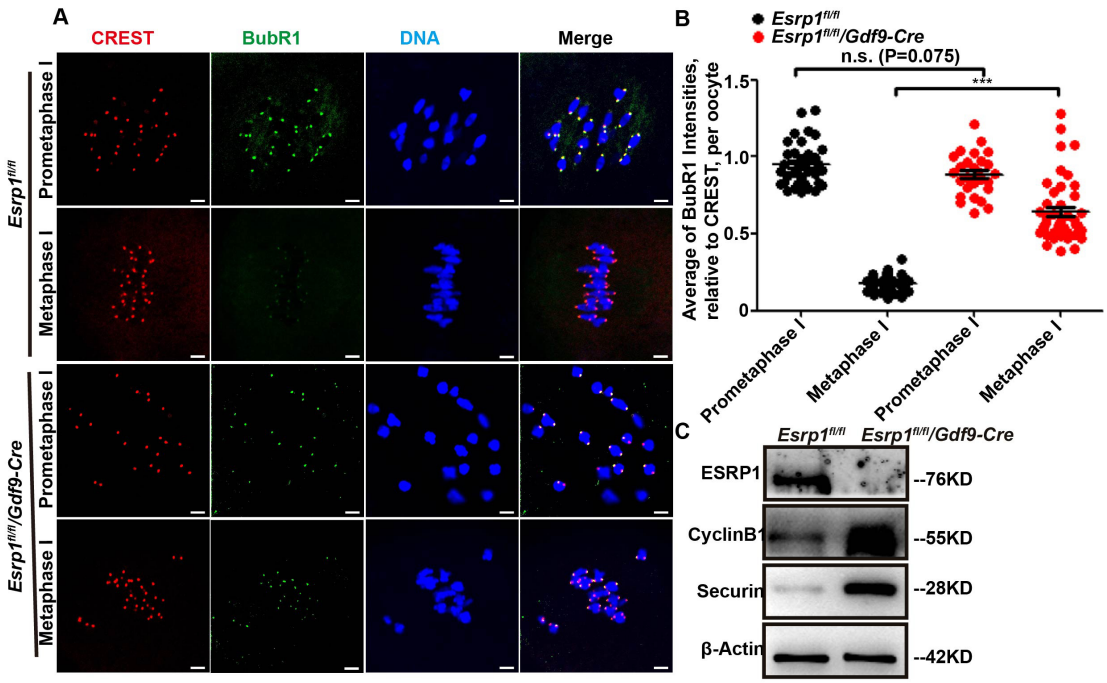

960

961 **Figure 5. *Esrp1* knockdown activates SAC and induces insufficient APC/C**
962 **activity** (A) Chromosome spreads were prepared 4 h (prometaphase-I) and 6 h

963 (metaphase-I) after GVBD in oocytes of *Esrp1*$^{fl/fl}$ and *Esrp1*$^{fl/fl}$*/Gdf9-Cre* mice, then
964 stained with CREST (red), BubR1 (green) and DAPI (blue). Scale bar, 5 μm. (B)
965 Quantification of BubR1 signal intensity relative to CREST; each point is the relative
966 intensity across centromeres. Data from prometaphase-I *Esrp1*$^{fl/fl}$ oocytes (0.95 ± 0.02)
967 and *Esrp1*$^{fl/fl}$ */Gdf9-Cre* oocytes (0.88 ± 0.03) are shown. Metaphase-I *Esrp1*$^{fl/fl}$
968 oocytes (0.18 ± 0.01) and *Esrp1*$^{fl/fl}$ */Gdf9-Cre* oocytes (0.64 ± 0.03) are shown (***P
969 < 0.001). (C) Western-blot analysis of Cyclin B1 and Securin in oocytes collected
970 after 10 h in culture from *Esrp1*$^{fl/fl}$ and *Esrp1*$^{fl/fl}$*/Gdf9-Cre* mice. β-actin served as a
971 loading control. Experiments were repeated at least three times; representative images
972 are shown.

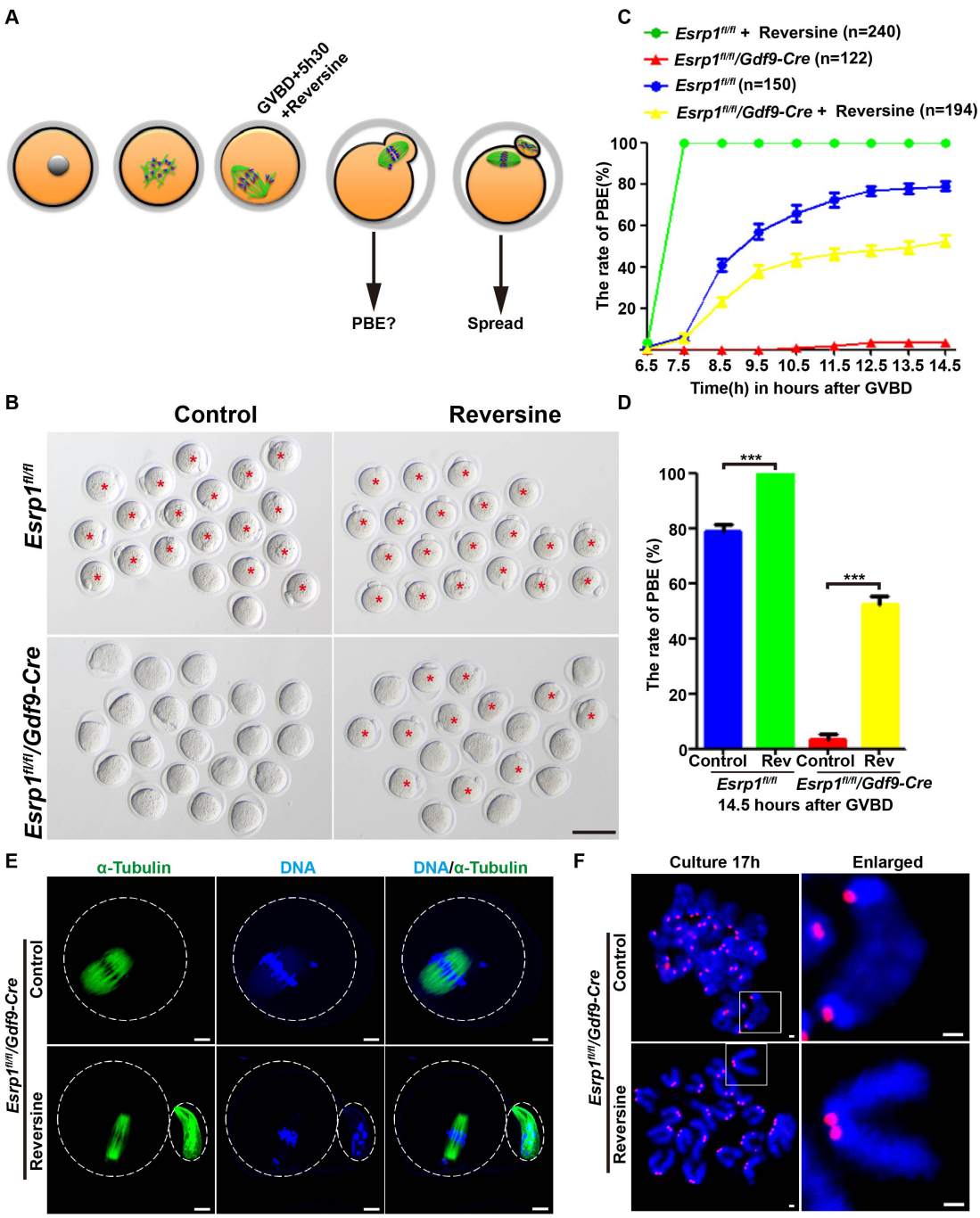

Figure 6. Metaphase-I arrest in *Esrp1*-knockout oocytes is rescued via inhibition of SAC activity. (A) Oocytes were treated with reversine (0.5 μM) at the indicated time to override a potential SAC arrest. (B) DIC imaging of *Esrp1*$^{fl/fl}$ and *Esrp1*-knockout oocytes treated with reversine shows that they completed the first meiosis, as determined by PBE cultured for 16.5 h. The asterisk indicates PB1. Scale bar, 100 μm. At least three independent experiments involving a total of at least six mice were performed. (C) Time of PBE of *Esrp1*$^{fl/fl}$ and *Esrp1*$^{fl/fl}$*/Gdf9-Cre* oocytes.

981 Reversine was added at GVBD+5.5 h, where indicated. n: number of used oocytes.
982 (D) Statistical analysis of the PBE rates of oocytes shown in (B). Data from *Esrp1*$^{fl/fl}$
983 oocytes (control: 78.96% ± 2.31%) and (reversine: 100%) are shown. Data from
984 *Esrp1*$^{fl/fl}$ */Gdf9-Cre* oocytes (control: 3.49% ± 1.78%) and (reversine: 52.58%± 2.51%)
985 are shown (***P < 0.001). Abbreviations: rev: reversine. (E) Immunofluorescent
986 staining with α-tubulin to visualize spindles (green) and co-stained with DAPI to
987 visualize chromosomes (blue) show *Esrp1*-knockout oocytes had extruded PB1 after
988 reversine treatment. Scale bar, 10 μm. (F) Oocytes were spread 17 h after culture.
989 Kinetochores were stained with CREST (red) and chromosomes with DAPI (blue).
990 *Esrp1*-knockout oocytes had entered to metaphase II with univalent sister chromatids
991 after reversine treatment. Insets show typical chromosome figures observed. Scale bar,
992 1 μm.

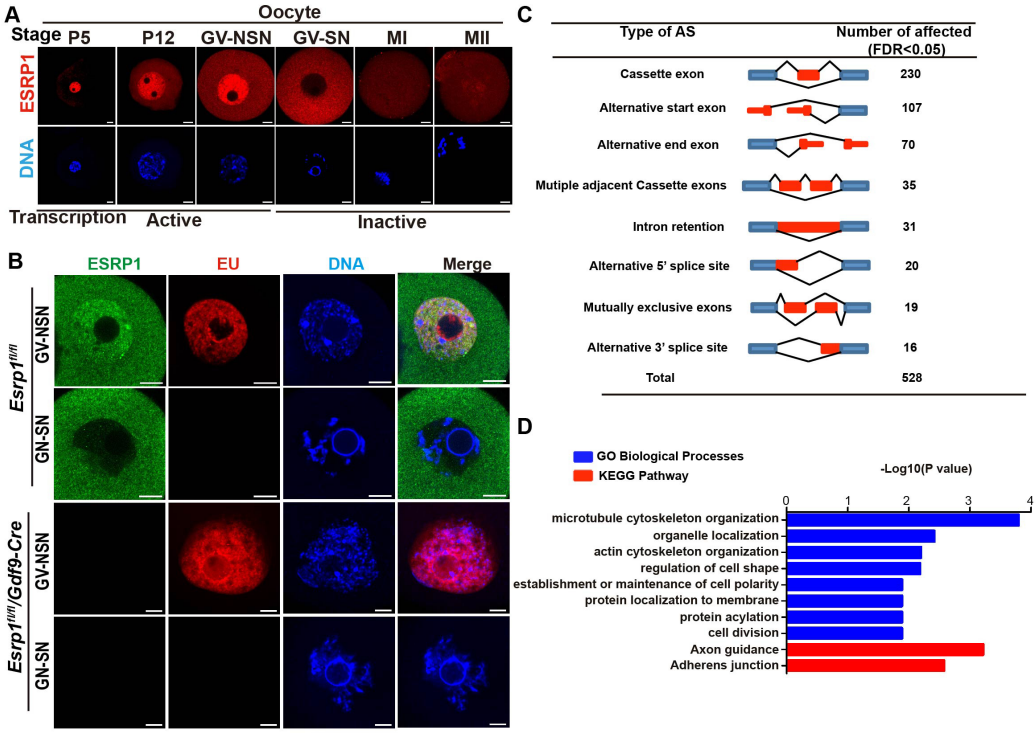

993

994 **Figure 7. Preferential nuclear-localized ESRP1 is involved in oocyte mRNA**
995 **processing.** (A) Immunofluorescence showing localization of ESRP1 (red) in oocytes.
996 DNA was stained with DAPI (blue). Abbreviations: P5, P12: postnatal days 5, 12; GV:
997 germinal vesicle stage; NSN: non-surrounded nucleolus; SN: surrounded nucleolus;

998 MI: metaphase I; MII, metaphase II. Scale bars, 10 μm. (B) Co-staining of 5-EU (red)
999 and ESRP1 (green) in mouse oocytes in NSN- and SN-nucleolus types at GV stages.
1000 DNA is shown in blue. Scale bars, 10 μm. (C) Diagrams of eight AS events
1001 recognized by CASH software and splicing events were significantly affected by the
1002 depletion of *Esrp1* in ovulated oocytes analyzed via RNA-seq data using CASH
1003 software (FDR<0.05). (D) GO-term enrichment and KEGG-pathway analyses of
1004 genes with significantly affected AS events.

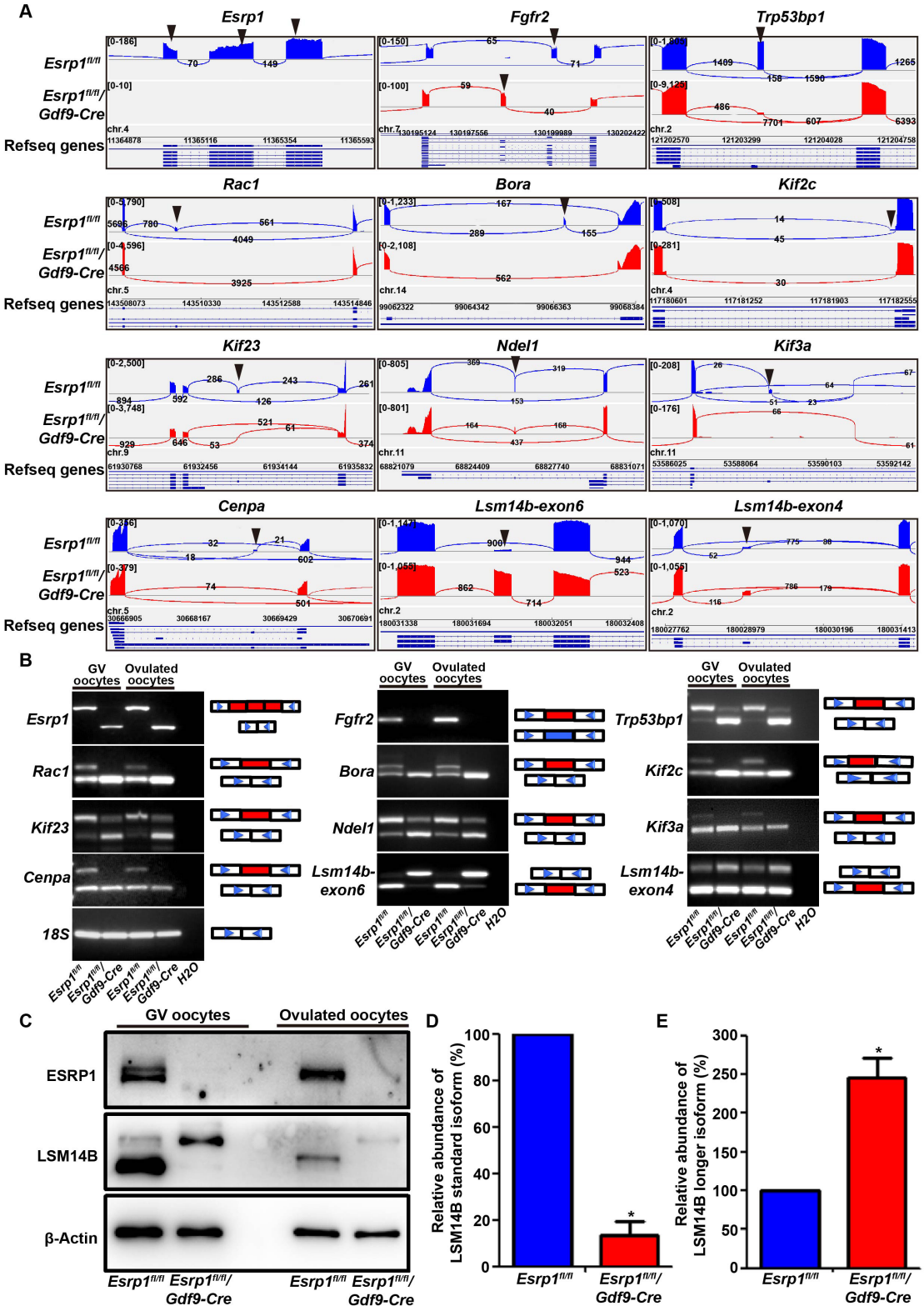

Figure 8. Loss of ESRP1 in oocytes leads to global changes in pre-mRNA splicing

(A) Use of IGV software shows alternative sites in genes related to oocyte spindle organization, as indicated from RNA-seq results. Black arrowheads indicate splicing sites. (B) PCR analysis of AS patterns of the changed spliced genes in GV-stage and

1010 ovulated stage oocytes from *Esrp1*$^{fl/fl}$ and *Esrp1*$^{fl/fl}$*/Gdf9-Cre* mice. 18s served as the
1011 internal control. PCR was performed with specific primers (Table S1) from three
1012 independent experiments. (C) Western-blot analyses showing the expression of two
1013 isoforms of LSM14B in GV-stage and ovulated stage oocytes from *Esrp1*$^{fl/fl}$ and
1014 *Esrp1*$^{fl/fl}$*/Gdf9-Cre* mice. β-actin served as a loading control. (D–E) Relative
1015 abundances of LSM14B standard and longer isoforms in GV-stage oocytes from
1016 *Esrp1*$^{fl/fl}$ and *Esrp1*$^{fl/fl}$*/Gdf9-Cre* mice were measured by Western-blot analyses from
1017 three independent experiments (*P < 0.05).

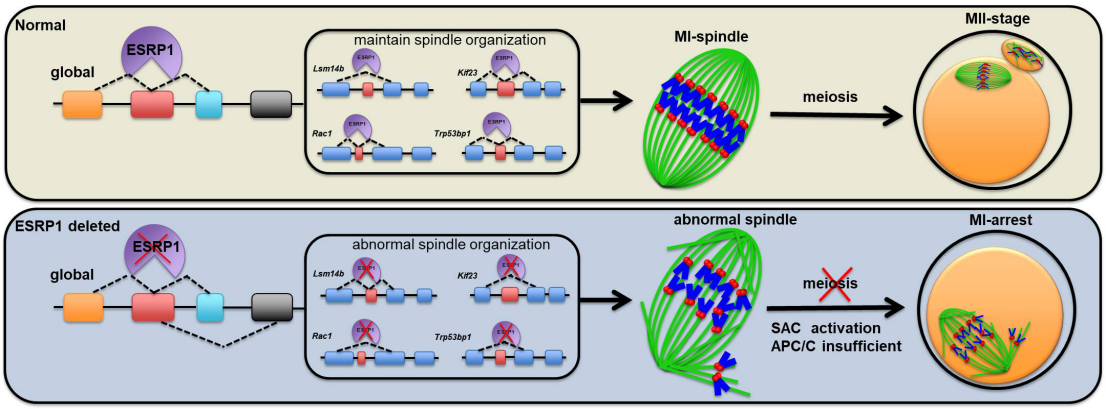

1018

1019 **Figure 9. Proposed schematic model of ESRP1 function during oocyte meiotic**
1020 **progression.** Generally, in normal oocytes, post-transcriptional modification of the
1021 maternal store mRNAs via AS and correct splicing promote to form typical
1022 barrel-shaped spindles and well-aligned chromosomes on the metaphase plate, leading
1023 to PBE and completion of the first meiosis. However, deletion of ESRP1 in oocytes
1024 leads to compromised global maternal mRNA splicing, which then leads to severe
1025 spindle organization defects, chromosomes misalignments, which contribute to
1026 abnormal activation of SAC and insufficiency of the APC/C. Hence, *Esrp1*-knockout
1027 oocytes failure to extrude the PB1 and are arrested at metaphase I.

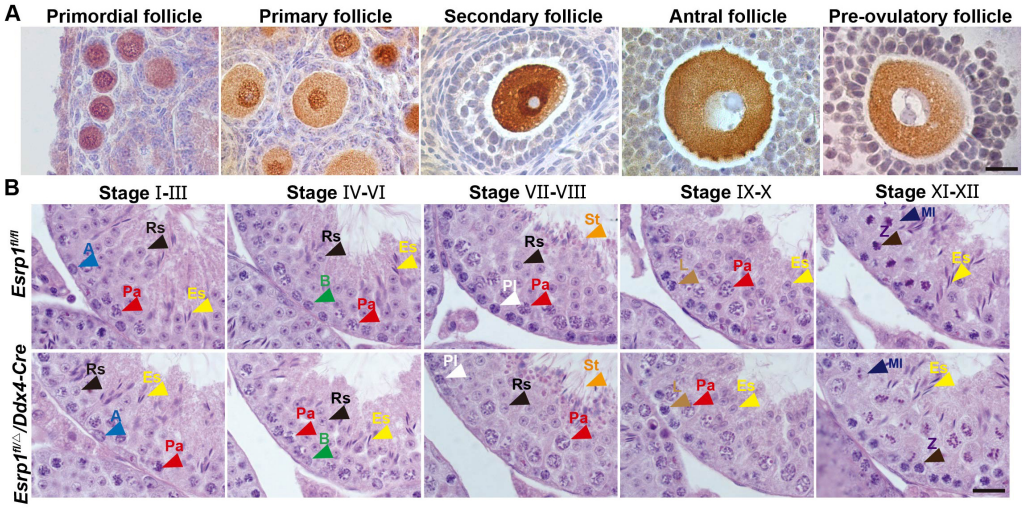

1028

1029 **Figure S1. Expression and subcellular localization of ESRP1 during follicular**

1030 **development.** (A) An immunohistochemistry (IHC) of ESRP1 in ovarian sections

1031 showing ESRP1 expression in follicles at indicated developmental stages. Scale bars,

1032 20 µm. (B) HE staining of adult *Esrp1*$^{fl/fl}$ and *Esrp1*$^{fl/\triangle}$*/Ddx4-Cre* testicular sections.

1033 Scale bars, 20 µm. Abbreviations: A: Type A spermatogonia; B: Type B

1034 spermatogonia; PI: Preleptotene spermatocyte; L: Leptotene spermatocyte; Z:

1035 Zygotene spermatocyte; Pa: Pachytene spermatocyte; MI: Post-prophase I meiotic

1036 phase; Rs: Round spermatid; Es: Elongated spermatid; St: spermatozoa.

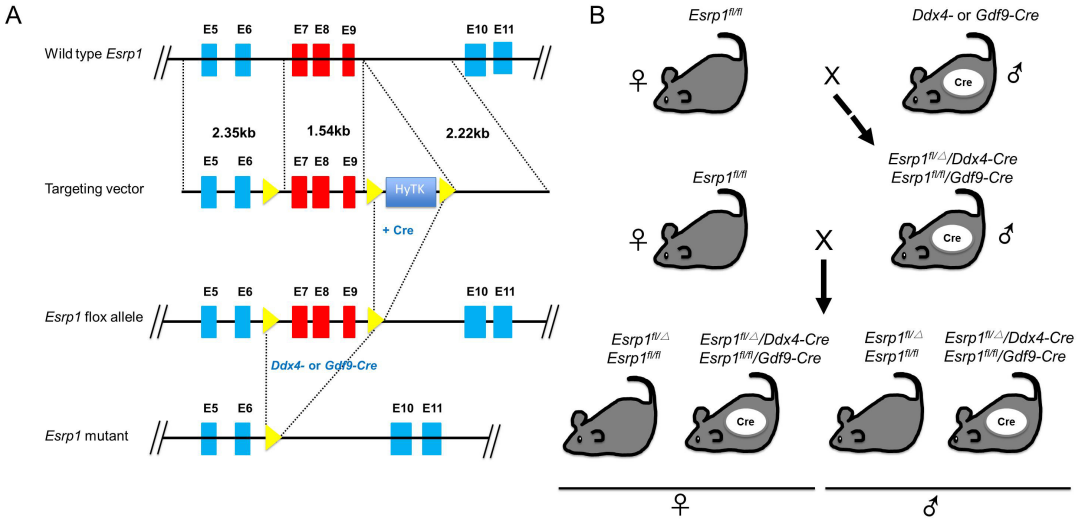

1037

1038 **Figure S2. Generation of *Esrp1* conditional-knockout mice.** (A) Construction of

1039 *Esrp1*$^{Flox/Flox}$ and generation of *Esrp1*$^{fl/\triangle}$*/Ddx4-Cre* and *Esrp1*$^{fl/fl}$ */Gdf9-Cre* mice.

1040 Exons 7–9 of *Esrp1* were deleted by *Ddx4-Cre*-mediated or *Gdf9-Cre*-mediated

1041 recombination. (B) Schematic of the breeding scheme to produce PGCs-specific

1042 *Esrp1* knockout in *Esrp1*$^{fl/\triangle}$*/Ddx4-Cre* mice and oocyte-specific *Esrp1* knockout in

1043 *Esrp1*$^{fl/fl}$ */Gdf9-Cre* mice.

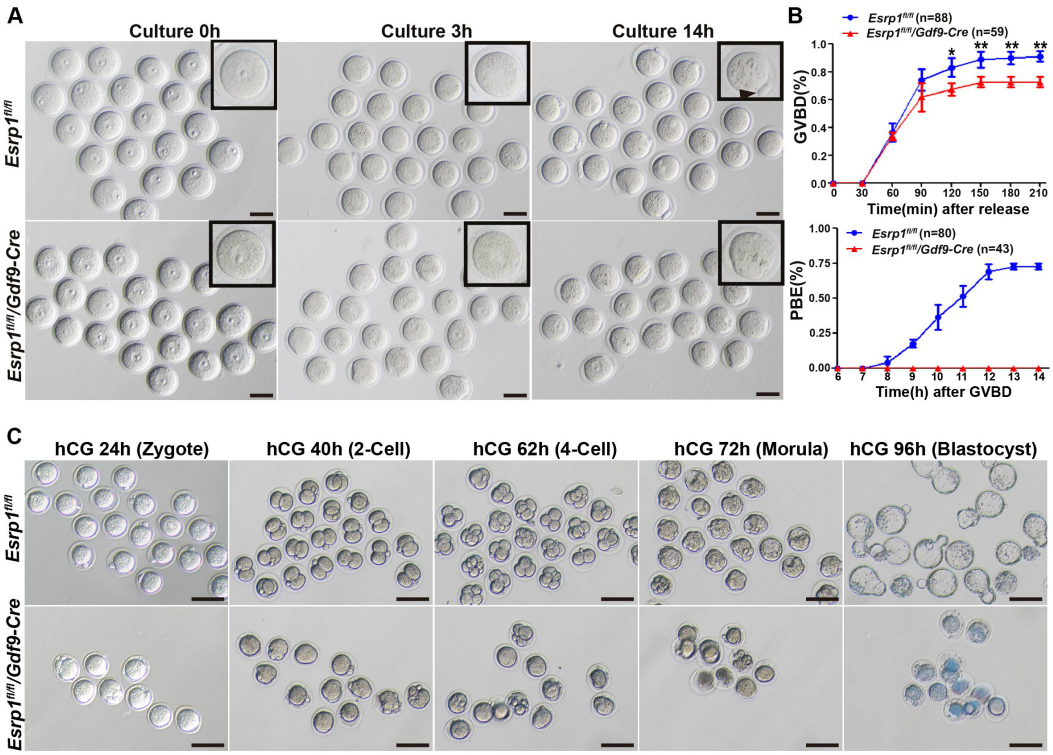

1044

1045 **Figure S3. Compromised meiosis and embryonic development in *Esrp1*-**

1046 **knockout oocytes.** (A) DIC imaging of the progression of meiosis in *Esrp1*$^{fl/fl}$ and

1047 *Esrp1*$^{fl/fl}$*/Gdf9-Cre* oocytes in culture. Time indicates hours after oocytes were

1048 released from meiotic arrest. Scale bar, 100 mm. (B) GVBD and PBE rates of

1049 cultured oocytes shown in (A). n: number of used oocytes. (C) DIC imaging of

1050 *Esrp1*$^{fl/fl}$ and *Esrp1*$^{fl/fl}$*/Gdf9-Cre* female embryos cultured *in vitro*. Embryonic

1051 development was monitored at the indicated time points after hCG administration.

1052 Scale bar, 100 μm.

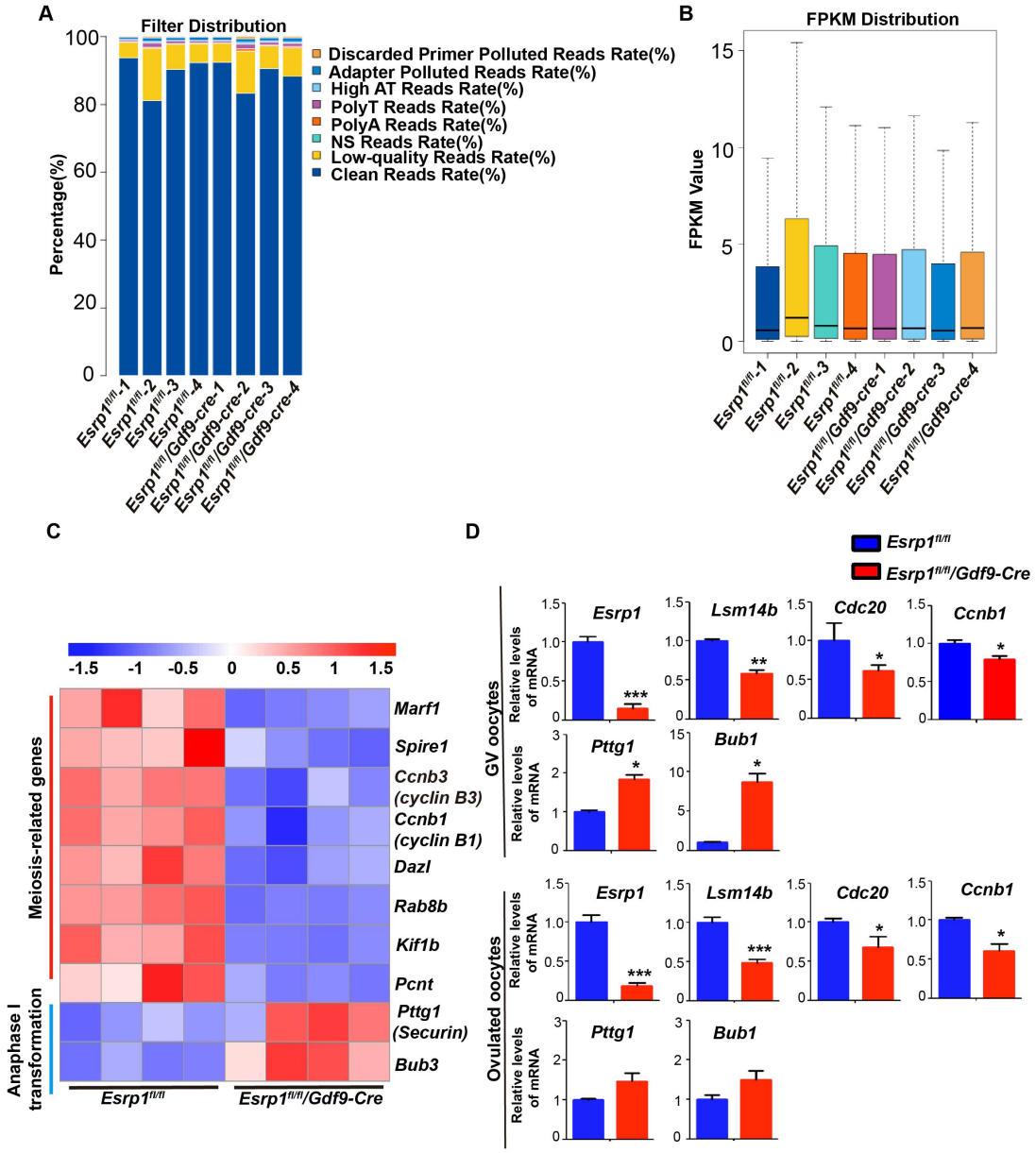

Figure S4. ESRP1 regulates mRNA transcription involved in oocytes meiosis. (A) Filter distribution in each sample; the clean reads were filtered for analyses. (B) Distribution of global gene expression in each sample. (C) A heatmap showing the transcript level of key genes that were involved in meiosis in *Esrp1*$^{fl/fl}$ and *Esrp1*$^{fl/fl}$*/Gdf9-Cre* oocytes. The color indicates the expression level. (D) Real-time RT-PCR analysis of mRNA levels of a cohort of genes. The mRNA levels of *Esrp1, Lsm14b, cdc20,* and *Ccnb1* were decreased in both GV-stage and ovulated oocytes from *Esrp1*$^{fl/fl}$*/Gdf9-Cre* mice compared to those in *Esrp1*$^{fl/fl}$ mice. The mRNA levels of *Bub1*and *Pttg1* were increased in both GV-stage and ovulated oocytes from

1063 *Esrp1*$^{fl/fl}$/*Gdf9-Cre* mice compared to those in *Esrp1*$^{fl/fl}$ mice. (*$p < 0.05$, **$p < 0.01$

1064 and***$p < 0.001$).

1065

1066

1067

1068

1069

1070

1071

1072

1073

1074

1075

1076

1077

1078

1079

1080

1081

1082

1083

1084

1085